Reply to reviews of manuscript „High-resolution modelling of early contrail formation behind hydrogen-powered aircraft”

We thank both reviewers for their thoughtful and constructive comments. Their feedback stimulated valuable internal discussions regarding the approaches used in this study. We hope that incorporating the aspects highlighted by the reviewers has helped improve the manuscript's overall quality. Below, we address all points raised by the reviewers and provide additional information where necessary. The reviewer’s comments are in normal font, *and our replies are in italics*. Changes in the manuscript text are in green.

As a first step, we include the figure and accompanying section on the evolution of temperature and humidity in the (x,z)-plane, as suggested by the editor Dr. Yu. The following figure and paragraph have been added to the supplementary material:

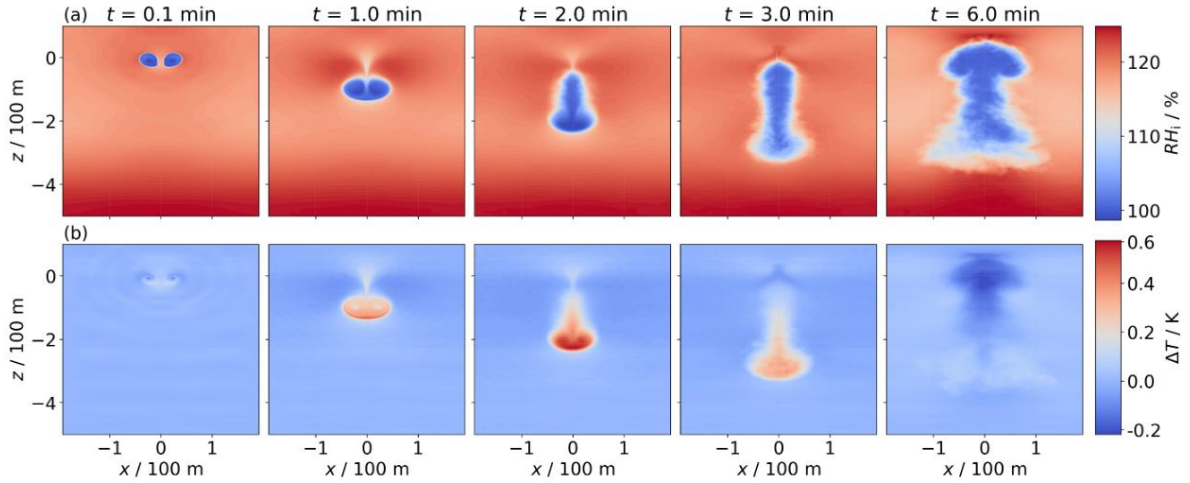

Figure S1. Temporal evolution of relative humidity with respect to ice (a) and temperature difference (b) in the x, z-plane (averaged along flight direction). In (b), the vertical background temperature profile is subtracted to highlight the temperature evolution, particularly within the primary wake. Note that the first column corresponds to 0.1 min, whereas the zeroth time step is shown in the main body of the manuscript. This distinction is made because the thermodynamic fields exhibit almost no visible features at the initial time step. The depicted exemplary simulation is performed for an A350/B777-like aircraft at $T_{\mathrm{CA}} = 217\,\mathrm{K}$, $RH_{\mathrm{i,amb}} = 120\,\%$, $N_{\mathrm{BV}} = 1.5 \times 10^{-2}\,\mathrm{s}^{-1}$, $N_0 = 3.38 \times 10^{12}\,\mathrm{m}^{-1}$, $I_0 = 15.0\,\mathrm{g\,m}^{-1}$, and $r_{\mathrm{SD}} = 3.0$.

Figure S1 illustrates the evolution of ice relative humidity (a) and temperature difference (b), where the background temperature profile has been subtracted. Within the wake vortices, the ice relative humidity remains close to saturation until the vortices dissipate. This phenomenon results from the sublimation of ice crystals trapped in the primary wake. The sublimation increases the local water vapor concentration, balancing the decrease in RH_i caused by adiabatic heating. Note that humidity values below 100% may occur as the sublimation does not instantaneously relax the humidity field to saturation. In the secondary wake, RH_i also remains near saturation as detrained ice crystals deplete ambient moisture, reducing the environmental supersaturation toward saturation. The presented humidity fields are quite smooth as they are averages along flight direction.
Initially, the temperature perturbation is nearly everywhere close to zero. The centers of the wake vortices feature a pressure drop to compensate for centrifugal forces and can lead to a very localized temperature drop. Due to the prescribed stable stratification, air masses at the original flight altitude have a higher potential temperature than air masses beneath. Hence, the descending primary wake is identified by positive ΔT values.

A similar consideration explains the negative ΔT values after six minutes around z=0 m. Air masses from the primary wake rise back to the initial altitude and push or contain also air masses from lower altitudes (with lower potential temperature) to z=0 m leading to ΔT<0 K.

We noticed that both reviews primarily focus on the representation of dynamics in our model. It is important to emphasize that a series of sensitivity studies—examining grid resolution, initialization, and wake vortex dynamics—have already been conducted and published in previous works (Unterstrasser et al., 2014, ACP; Unterstrasser et al. 2014, JGR; Unterstrasser & Görsch 2014, JGR, Unterstrasser & Stephan, 2020). In the current study, we adopt the same configuration with respect to domain size, resolution, and wake vortex characteristics, while focusing on a detailed investigation of microphysical variations. Importantly, the dynamical setup remains unchanged from these earlier studies.
We also stress that the resolution requirements depend on the application. For example, in studies of hazardous wake vortex encounters, the erosion of the vortex core is critical, as it influences peak velocities and rolling moments. In contrast, for contrail simulations, the key dynamical feature is the final vertical displacement of the vortex system, which determines the vertical extent of the contrail and the magnitude of adiabatic heating.
The robustness of our dynamical model has been addressed in several previous studies. For instance, comparisons between NTMIX, a higher-order code, and our model EULAG-LCM show very similar results for the vertical tracer distribution after wake vortex breakup, when thermal stability and ambient turbulence are varied (Unterstrasser et al., 2014, ACP, Figure 15). A broader intercomparison of contrail LES models (Unterstrasser, 2016, Figure 13) showed excellent agreement in vortex descent predictions, with discrepancies limited to one outlier model in terms of ice crystal loss.
A more recent study with EULAG-LCM focused on the early contrail evolution behind a formation of two aircraft. In this application, the flow field is characterized by complex interactions between four wing-tip vortices, and the dynamical patterns differ strongly from the classical scenario of a descending wake vortex pair behind a single aircraft. In that study (Unterstrasser & Stephan (2020)), grid sensitivity studies and intermodel comparisons were conducted to evaluate the dynamical part of the simulations. EULAG-LCM was compared to MGLET, a model widely used in wake vortex studies (e.g. Misaka et al., 2012; Misaka et al., 2015, Stephan et al., 2017), and a good agreement was found. Importantly, sensitivity studies on grid resolution have also been conducted. For example, simulations with longitudinal resolutions (along flight direction) of 2 m, 1 m, and 0.5 m (Unterstrasser & Stephan, 2020) showed only minor differences in ice crystal profiles, with survival fractions differing by less than 5%.

These points demonstrate our awareness of testing the robustness of the dynamical model. Sensitivity analyses on grid resolution have not only been performed, but EULAG has also been benchmarked against other established LES models to validate its performance. Nonetheless, as mesh resolution was among the primary concerns raised in the review, we repeated one of the simulations with a finer grid. Additionally, a sensitivity analysis of the domain width was carried out in response to a related reviewer comment. The results confirm that both the original resolution and domain width are sufficient to capture the relevant dynamics. The outcomes of these additional sensitivity tests are included in the supplement, and a more detailed discussion is provided below.

Additionally, minor revisions, primarily related to grammar and spelling, have been made to the manuscript. While these changes are not individually detailed in this document, they are fully visible in the manuscript version with tracked changes.

Review 1

Dear reviewer,

We are grateful for your comments and suggestions. Your feedback has been very helpful in improving the quality of our paper. We hope that the new version adequately addresses your concerns. Below, we explain how we tackled your comments.

General comment:
The aim of this paper is to present a new parametrization for ice crystal lost during contrail vortex phase. More than just a parametrization, a lot of 3D simulation has been performed in order to have a sensitivity analysis to the apparent ice crystal number emission index and to water emission index in order to include what could be expected from a H2 combustion engines or fuel cells. This has been made by increasing or decreasing the number of ice crystals from the one of a usual kerosene jet engine by 1 and 2 order of magnitude and using the adapt water emission for an H2 engine. I think this approach is totally valid considering the lake of knowledge on H2 contrails.
First, the computational methodology is described in detailed. Then a physical analysis of the results is made with several sensitivity analysis bringing good understanding of the physics. Then the parametrization is presented and compared to their CFD results (from this study and from a past one). The comparison between the parametrization and the CFD results are convincing and the paper shows an improvement compared to the previous parametrization.
On the improvement of the parametrization by itself, I think the paper present good results which can justify by itself the publication. The paper is well written and gives a lot of information. However, I think it would gain in clarity for the reader with less knowledge if some information on the past parametrization are given. I have regroup what, in my opinion could be added in order to improve the paper into the minor comments section of the present document.

> *Thank you very much for the summary of our work. We would like to emphasize that the primary objective of this study is a systematic investigation of young "hydrogen contrails" across a wide range of atmospheric parameters. The impact of the two key input parameters, initial number of ice crystals and initial water vapor emission, on the subsequent evolution into contrail-cirrus is demonstrated through exemplary cases. The updated parameterization of crystal loss is undoubtedly an important component of the manuscript.*

My main concerned are about the CFD by themselves that are may be in a too small domain, see mainly the major comment 1,2 and 5. In addition the considered initial condition may also introduced a modification of the survival ice crystals number (major comment 3). The major comment 4 is mainly here to increase clarity but, in my opinion, the information is important to be given. Therefor I will recommend 2 or 3 more computations. 1 with the same initial condition but with a bigger computational domain, made in such a way to leave more space above the contrail at the end or the vortex phase (comment 5) and more space at the left and right, in order to go under 1% of error on the vortex descent velocity (comment 1). Another one with your initial mesh with a gaussian plume surrounding the vortex core (almost no ice crystals in the vortex core). And one with a thinner discretization in order to the if there is no too much numerical dissipation in the vortices could be a good addtion. The comparison of the contrail evolution and the ice crystal survival fraction could be made in order to evaluate these influences. Since, I think, the paper is long enough, this can be added in an annex with a reference to it in the core text. In addition, I will say that the considered case for these simulations should be where the survival ice crystal fraction has an evolution so around a zd between 1 to 2.
On that regard I do not recommend publication on that stage, even if I think that this paper present great quality. I just want to make sure that no surprise arrive when using a better mesh, and with

another choice of initialization, and since Comment 1 and 3 could bring opposite effect on the survival ice crystal number, it could be great to see if and at what degree.

Thank you for your suggestions! We address each of the points in more detail below.

Major comments:

1. For the A350 you have a domain width of 384m. Assuming periodic boundary condition, it means that at initial time, you have an infinity (let assume 6, the 2 computed and the images at the left and at the right) vortices lines up on the x axis. Using point like vortex theory, you can compute the vortex descent velocity in the 6 vortices case and compare it to the 2 vortices that you want to compute. If Γ is the circulation of the vortex (520 m²/s), b the separation length of your 2 vortices and L the size of your computational domain (384m), the theoretical descent velocity of the vortex pair is given by $V_t = \Gamma/2\pi b$ wherease, taking into account the 4 other vortices, the descent velocity in your computation should be given by $V_c = \Gamma/2\pi b - \Gamma/2\pi(L-b\,2) + \Gamma/2\pi(L+b\,2) - \Gamma/2\pi L + \Gamma/2\pi(L+b)$. (I don't think so but I may have make some mistakes so please validate or not this formula). Using your values I find Vc=1.7m/s and Vt=1.75m/s, this mean an error of 3%. In https://doi.org/10.5194/acp-15-7369-2015 , the authors use a 1km domain and not only 384m (error of 0.5%). The span of their aircraft is kind of the same, however the circulation is a bit higher, still the relative error doesn't depend of the circulation. Since the descent of the vortices may affect the position of your ice crystals, it may also affect the ice crystal loss and therefore your parametrization. Your comparison with this mentioned paper show that your parametrization is always under their results and only two cases of Lewellen 2014 is under and he also has an error in descent velocity under 1%. Could you look at the influence of the domain size in transvers direction by doing a simulation with 1km in the reference stratification case and a configuration with a zd around one or 2 (it seems to be most challenging).

Your comment is greatly appreciated. We want to clarify that, in our model, the initial velocity field of the vortex pair is not continued across the boundary in the transverse direction. Therefore, no mirror vortices—of the kind you described—are present, and no initial interactions between such mirror vortices and the primary vortex pair occur. That said, due to the use of periodic boundary conditions in the transverse direction, it is true that interactions could theoretically arise if the vortices undergo strong oscillations (e.g., due to Crow instability) during the simulation. This is precisely why the simulations with lower stratification values use a larger domain in the transverse direction, as stronger vortex oscillations are observed.

To make sure that such cross-boundary interactions do not severely alter the final survival fraction of ice crystals, we repeated one baseline simulation with a doubled domain size in the transverse direction as you proposed. Using a larger domain width, we observe a 0.5% variation in the ice crystal survival fraction.

In Section 3 of the supplement, Figure S6 shows the temporal evolution of ice crystal mass and number of the reference and the larger-domain simulation [also a simulation conducted at a higher pressure level is shown]:

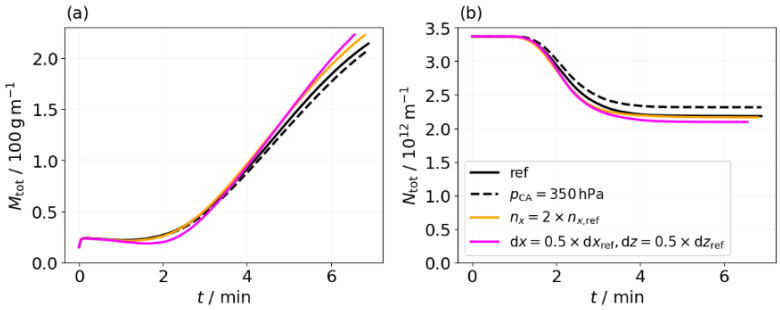

Figure S6. Evolution of total ice crystal number (a) and total ice mass (b) for the reference case and three sensitivity simulations, differentiated by color and line style. The dashed black curves represent a simulation conducted at a higher ambient pressure value. The orange curves correspond to a simulation with doubled domain width. The magenta curves show the results from a simulation with a higher mesh resolution in transverse and vertical direction.

We included the following paragraph into Section 3.2 of the supplement:

The default domain size in the transverse direction is 384 grid boxes, corresponding to 384 m in our reference A350/B777 simulation with a grid spacing of dx = 1 m. In a sensitivity simulation, we increase the domain width from 384 m to 768 m; the results are shown as orange curves in Fig.S6. This modification yields a slight reduction in final ice crystal survival fraction from 64.7% to 64.2% and a relative increase of 4.6% in final ice mass.
A plausible explanation is that, in the narrower domain, the descending vortex pairs might interact across the transverse boundaries, damping their descent and thereby enhancing ice crystal survival. Horizontal profiles reveal that, from about two minutes onward, the wider-domain simulation exhibits slightly lower ice crystal number and mass near the outer edges of the vortices, while more ice crystals and ice mass are found in the vortex centers. This supports the hypothesis that transverse interactions across the boundaries in the narrow domain might influence vortex dynamics and particle motion.
However, it is equally plausible that the minor deviations in the evolution of ice crystal number and mass reflect variability introduced by background turbulence, as discussed in the previous section.
As the wider domain has a negligible effect on the contrail properties, most notably the ice crystal survival fraction, yet significantly increases computational expense, a transverse width of 384 grid boxes is deemed sufficient for our simulations.

Regarding your point on the differing survival fractions compared to the LES results of Picot et al., 2015, we believe these discrepancies can be attributed to the exclusion of the Kelvin effect in their study. Including the Kelvin effect leads to lower survival fractions as the growth of small ice crystals is hampered. The importance of the Kelvin effect on contrail evolution has been mentioned in several studies (Lewellen 2012 and Lewellen 2014). Moreover, Figure 13 of Unterstrasser 2014, JGR shows substantially higher survival fractions if the Kelvin effect was deliberately switched off.

2. Your mesh resolution is 4 to 5 points in the core radius of the vortices (as in https://doi.org/10.5194/acp-15-7369-2015. In https://doi.org10.1017/S002211209600849X it would be more 10 points and in https://doi.org/10.1063/1.4934350 it is about 8 meaning about twice as much points by radius core as yours. Have you done (for this paper or in the past) a sensitivity analysis to this parameter?

Thank you for bringing this to our attention. A sensitivity study to the grid resolution has been performed by Unterstrasser et al., 2014, ACP, where the resolution in the flight direction was refined from 2 m to 1 m. Their results indicate that the resolution in flight direction has no significant influence on the final contrail properties. As explained above, a grid sensitivity analysis has also been performed in Unterstrasser & Stephan, 2020.
To specifically address the impact of grid resolution within the vortex cores, we conducted an additional sensitivity simulation in which the default mesh resolution of 1 m in both, transverse and vertical directions was refined to 0.5 m (in the A350/B777-like aircraft case). While the outcomes indicate that mesh resolution does have some influence on contrail evolution, its impact remains minor compared to other parameter variations considered in this study.

In the supplement, Figure S6 shows the temporal evolution of ice crystal mass and ice crystal number of the high-resolution simulation compared to the reference simulation. We included the following paragraph into Section 3.1 of the supplement:

In the reference setup, we employ a horizontal and vertical grid spacing of 1 m. To assess the sensitivity of contrail evolution to mesh resolution, we conduct an additional simulation using a finer resolution of 0.5 m. As shown by the magenta curves in Fig.S6, the higher-resolution simulation results in a relative increase of 7.7% in total ice mass and a reduction in ice crystal survival fraction from 64.7% to 62.1%.
Vertical profiles of ice crystal number and mass (not shown) indicate that, in the high-resolution setup, fewer ice crystals are detrained from the vortex system. Instead, a larger fraction remains trapped within the primary wake, where they are more prone to sublimation due to adiabatic heating.
The reduced detrainment can be attributed to the way secondary vorticity, generated by baroclinic torque arising from density and pressure gradients between the wake and the ambient air (Holzäpfel et al., 2001), develops in the simulation. Although the underlying physical conditions, such as pressure and density gradients, remain unchanged, the finer grid spacing enables a more accurate resolution of these instabilities, potentially altering the dynamics of vortex destabilization. We hypothesize that the improved representation of secondary vorticity results in less disruption of the vortex cores, thereby reducing ice crystal detrainment and increasing sublimation within the primary wake.
Alongside this physical explanation of the observed results, we note that background turbulence could likewise influence the detrainment process and contribute to the observed behavior.
While the resulting discrepancies in ice crystal number and mass are moderate compared to those induced by variations in the initial ice crystal number, they underscore the relevance of mesh resolution and its potential impact on simulation outcomes. However, in the context of a sensitivity study focused on variations in initial ice crystal number, where ice crystal survival fractions span the full range from 0 to 100%, we consider deviations in ice crystal survival fraction below 3% to be minor. Given the substantial computational demands of finer mesh resolutions (roughly eight times higher CPU time) and considering the comparatively minor differences in simulation outcomes, we consider the baseline resolution appropriate for the objectives of this study.

3. The discs present a constant ice crystal number, however since the ice crystals are created outside the vortex core it will take some time for them to penetrate the vortex core since diffusion is probably the main process which can allow them to penetrate the core due to the

closed streamlines. For the same reason the ice crystals initially inside the vortex core are mainly trapped and will descent with the vortices. By this initialization choice, don't you increase artificially the number of ice crystals that remains in the primary wake and then the number of particles that sublimate? (As an example https://doi.org/10.1103/PhysRevFluids.8.114702, shows (in 2D case) that the position of the initial plume can have an influence on the vertical spreading of the contrail, and putting them inside the vortex core force them to stay inside the vortex core.)

> *Thanks for this comment. It is correct that we initialize the setup such that the discs of the ice crystals are aligned with the centers of the vortices. A sensitivity study on the initial spatial distribution of ice crystals was conducted in Unterstrasser et al., 2014, ACP. In that study, the radius of the plumes was varied (5, 15, 20, 25 m). Additionally, a ring-shaped distribution was used instead of a disc, and a non-uniform spatial distribution of ice crystals was tested. The results showed that while there are initial differences in the profiles, these differences diminish over time. Ultimately, the degree of mixing and the qualitative structure of the primary and secondary wake are very similar (except for the case with r = 5 m, which represents an extreme scenario). Stratification and relative humidity have a much stronger influence on the profiles. For this reason, we adopt the simplified initialization in the current study.*
> *Furthermore, Section 3.4 in Unterstrasser & Görsch, 2014 also examines variations in plume radius and the use of a Gaussian initialization (with either two or four plumes initially placed outside the vortex center—this is the same study as described in Unterstrasser, 2014 JGR but focuses on different aircraft types). Figure 7 there shows that Gaussian vs uniform distributions make little difference, while the aircraft type or the initial number of ice crystals has a much larger effect. These simulations are included in the ice crystal loss parameterization.*
> *The cited Saulgeot et al., 2023 study uses a 2D approach. It was compared to 3D model results, however, this was limited to an early stage of vortex stage and misses the phase where wake vortices break up due Crow instability (a vortex meandering phenomenon that cannot be resolved in 2D) and where only diffusive processes lead to a degradation of the wake vortices. Moreover, the study does not clearly demonstrate the resolution requirements for accurately predicting ice crystal loss, which is a central focus of our work. Notably, we have previously found substantial discrepancies in ice crystal loss estimates between 2D and 3D simulations (see Figures 2 and 4 in Unterstrasser, 2014, JGR).*

4. You gives different quantities such as P_{amb}, T_{amb}, RH_i, amb and a Brundt Vaisala frequency.

I guess the given value is at flight altitude whereas the pressure field follow the hydrostatic equation, and T in the atmosphere follow a constant Brundt Vaisala frequency? If so I guess it worth to be written for the non-specialist readers. Moreover, the choice of the relative humidity evolution with altitude is not trivial, since the mass fraction of water can fluctuate in order to impose a constant relative humidity with altitude, or one can keep the mass fraction of water vapor constant, or some other choice can be made… Please indicate what has been your choice in that matter.

> *Thank you for pointing this out. In the simulation, the ambient pressure is prescribed at the lower boundary of the simulation domain. Using the hydrostatic equation and assuming a vertically constant Brunt-Väisälä frequency, the pressure profile throughout the simulation domain is calculated. Temperature is also computed based on the hydrostatic equation. The equations defining the profiles of p, ρ_{air}, T, and θ are given in Eq. 2 of Clark & Farley (1984). The relative humidity is prescribed as constant throughout the entire simulation domain. As a result, the absolute humidity varies from 0.1 gm^{-3} at flight altitude to 0.15 gm^{-3} at the lower boundary of the simulation domain (assuming a temperature of 217 K at flight altitude and*

our standard values for p_o and N_{BV}). The corresponding mass fraction ranges between 0.0003 and 0.0004.

To make this clearer, we changed the paragraph

"Additionally, we investigate the influence of different atmospheric conditions on the evolution of contrail ice crystals. At the lower boundary of the simulation domain, the pressure is 250 hPa and the air density is roughly 0.4 kgm^{-3} changing with the prescribed ambient temperature. We use a background turbulence field with an eddy dissipation rate epsilon=$10^{-7}m^2s^{-3}$. Previous research has highlighted the importance of ambient temperature at cruise altitude, ambient relative humidity, and atmospheric stratification (described by the Brunt-Väisälä frequency) as key input parameters (Lewellen 2014a, Unterstrasser, 2016). We vary these parameters as outlined in Tab.1."

into

"Previous research has highlighted the importance of ambient temperature at cruise altitude T_{CA}, ambient relative humidity with respect to ice $RH_{i,amb}$, and atmospheric stratification N_{BV} (described by the Brunt-Väisälä frequency) as key input parameters (Lewellen 2014a, Unterstrasser, 2016). We vary these parameters as outlined in Tab.1.
At the lower boundary of the simulation domain, we prescribe an air pressure of p_0=250 hPa and an air density of approximately $\rho_{air,0}$=0.4 kgm^{-3}. For ambient temperature, we prescribe cruise-altitude values of T_{CA}=217, 225, 230, 233, and 235 K. The relative humidity with respect to ice is assumed to be constant throughout the entire simulation domain and set to 110 or 120%. We use a background turbulence field with an eddy dissipation rate of $\varepsilon=10^{-7}m^2s^{-3}$.
The pressure and temperature vertical profiles are computed for an atmosphere with a vertically constant Brunt-Väisälä frequency according to Eq.2 in Clark and Farley, 1984.
At cruise altitude, the resulting air pressure ranges from 231 to 235 hPa, depending on Brunt-Väisälä frequency and temperature. In Tab.1, an average air pressure value is provided.
It would seem appropriate to vary ambient pressure in combination with T_{CA} to reflect a change in flight altitude. However, a variation of pressure has only little impact on the simulated contrail properties as demonstrated in Sec.3.3 in the supplement. This is because the background water vapor mass concentration is independent of ambient pressure. Hence, we do not adapt p_0."

5. In fig 2 the ice crystals are going above the flight altitude. In the picture, it seems to go dangerously close to the boundary of the domain. Are the ice crystals stopped in their movement due to the presence of the boundary condition?

Thank you for this valuable comment. We prescribe rigid boundaries in vertical direction, meaning that any flux of ice crystals is prohibited across the boundaries. The issue you describe was indeed encountered in simulations with ambient temperatures of 230, 233, and 235 K, where ice crystals reached the upper boundary of the domain. To address this, we increased the vertical extent of the simulation domain—using 800 m instead of the default 600 m for the A350-like aircraft, and 634 m instead of 488 m for the A320-like aircraft. 600 grid points in the vertical should therefore be regarded as a default value, but it is adjusted depending on parameter settings such as stratification and temperature.

To make this aspect clearer, we included the following into Section 2.2:

Additionally, for high cruise-altitude temperatures (i.e. T_{CA}=230, 233, and 235 K), the vertical domain size was increased from 600 to 800 grid points for the A350, and from 856 to 1112 grid points for the A320.

Minor comments:

1. In lines 102-103 you say that in the LCM solver you use numerical particles which represent a certain number of physical particles. However I haven't found in the text how many numerical particles are used and how many physical particles are represented by them. Since you make a sensitivity analysis on the number of particles, is it the number of numerical particles which is reduced or their weigh (number of physical particles inside a numerical one). Moreover can you provide a reference on the number of numerical particles to have a good contrail representation? (may be this one: https://doi:10.5194/gmd-7-695-2014*?)*

Thank you for this thoughtful comment. You are right, we have not mentioned the role of the simulations particles when increasing the number of real ice crystals. Hence, we included the following into Section 2.1:

Each simulation particle (SIP) represents a certain number of real ice crystals (referred to as the weight of the SIP) with identical properties, such as size and mass.

The following sentence is added in Section 2.2:

Varying the number of ice crystals in the model is achieved by varying the weight of the SIPs, which keeps their total number roughly the same.

A sensitivity study regarding the number of simulation particles has been performed in Unterstrasser, 2014, ACP. There, the SIP number was varied between 23e6 and 223e6. The following plot shows the temporal evolution of SIP number (left) and ice crystal number (right). The ice crystal number evolution is not affected by the SIP number variation. Hence, we conclude that our default number of around 23xe6 SIPs is sufficient for a good contrail representation.

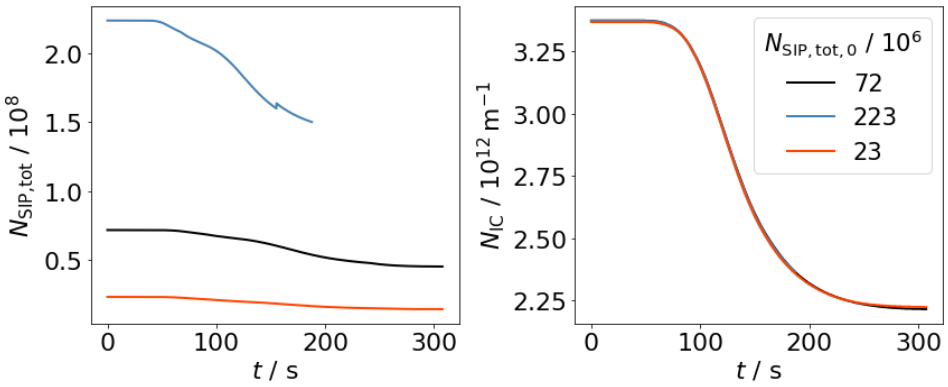

Moreover, Unterstrasser & Sölch (2014) conducted extensive tests on the numerical convergence properties of our particle-based approach. They demonstrate and argue why astonishingly few SIPs per grid box are needed to reach numerical convergence (note, however, that this publication analyzed contrail-cirrus simulations and not contrails during the vortex phase).

2. Line 105 you explain that some routine of LCM has been switched of such as aggregation and radiation. In 450 you add that sedimentation was also off for vortex phase. I think it worth noticing it also in line 105. Can you also provide either some reference or some order of magnitude in order to justify that you neglect tem?

Thank you for the comment.
Radiative processes are neglected in our simulations, as they act on significantly longer time scales (on the order of hours) compared to the time scales relevant in the vortex phase, which are on the order of a few minutes. The effect of radiation on contrail-cirrus was treated in Section 4 of Unterstrasser & Gierens, 2010 (Part 2) and in Lewellen, 2014a,b. The heating rates lead to changes over time scales of hours. However, they are negligible compared to the adiabatic heating and buoyancy effects during the vortex phase.
The probability for aggregation events to happen increases with increasing differential sedimentation velocities and increasing particle sizes (Sölch & Kärcher, 2010). Aggregation becomes significant when particle size differences exceed approximately 100 µm. Since such large differences in particle size do not occur during the vortex phase in our simulations, we deliberately switch off aggregation in our study.
Sedimentation is a process that we included in the vortex phase simulations. However, in Section 3.4, we mistakenly stated that sedimentation was turned off. To correct this, we have removed the following incorrect sentence from Section 3.4:

~~*While sedimentation was switched off in the vortex phase simulation, it is switched on here as it is a crucial process in the contrail-cirrus transition.*~~

3. In the paragraph from line 114 up to 123, you gives detailed of your mesh and boundary condition. You say that you use rigid condition for the vertical direction. At first glanced I have not really understood if you meant the xmin xmax (vertical normal) boundary or the zmin, zmax boundary (vertical plans). Please could you rewrite the lines 121 to 123 such that it will be blatant.

Thank you for pointing this out. With "rigid boundaries," we mean the zmin and zmax values. It means that no normal flux across the vertical boundary is allowed.
We added the following sentence into Section 2.2:

In the vertical direction, rigid boundary conditions are used, meaning that the vertical velocity component is zero at the top and bottom boundaries of the simulation domain.

4. You provide a lot of information about the initialization such as the plume radius which is represented by two discs. I have not find the position of the center of this discs. I imagine that it is center on the vortex center but please add the information in the text.

Thank you for your advice, this description is indeed missing in the text. We added the following sentence into Section 3.1:

The centers of the plumes and of the wake vortices are collocated on each side.

5. In the z direction, you have 600m which seems to go from -500m to 100m (on figure 2). Please put this information into the text.

Thank you for noticing that. We added this additional information in the caption of Figure 2:

The z-coordinate is shifted such that z=0 m corresponds to the cruise altitude (which is also done in Figs. 4, 5, and 6).

6. In your analysis you decrease the Brundt Vaisala to 0.005s-1. In https://doi.org/10.5194/gmd-5-543-2012 gives a typical range between 0.01 to 0.03. Is your parametrization has been tested for higher stratification levels? https://doi.org/10.5194/gmd-5-543-2012 gives a typical range between 0.01 to 0.03. Is your parametrization has been tested for higher stratification levels?

No, the default values that have been used throughout the present as well as the past studies have been 0.5e-2 and 1.15e-2 s^{-1}.
As shown in Dürbeck & Gerz, 1996, the distribution of N_{BV} values peaks around 0.01s^{-1} for tropospheric flight altitudes, with values exceeding 0.025 s^{-1} occurring only rarely. Clearly, stratospheric N_{BV} values are typically higher and peak at 0.02 s^{-1}. However, ice supersaturation is very rare in the stratosphere. Hence, our N_{BV} selection represents tropospheric conditions.
Moreover, in non-dimensional terms, N_{BV} is given by N_{BV} x t_0 (t_0 is the vortex time scale). This quantity varies over a wider range as t_0 changes with a variation of aircraft type. Figure 8 in Unterstrasser & Görsch (2014) depicts the non-dimensional vertical displacement z_{desc}* = z_{desc}/b_0 as a function of N_{BV}*, where data points with different t_0 values lie on one universal line. Hence, one may expect that the simulations cover implicitly a larger variation of N_{BV}.*

7. In your part 3.3 and in the annex you talk about the paper U2016 and tell this formula replace this formula from U2016 … I think the paper will gain in clarity if you write the formula from U2016

Thank you for this point. In the main body, we repeat the definition of z_{desc} so that all length scale definitions are given. Therefore, in Section 3.3, we add

We repeat the definition of z_{desc}, which is $z_{desc} = (8\Gamma_0/(\pi\, N_{BV}))^{1/2}$.

In A2, we now write:

In step 2, the formula for computing the plume area is now $A_p = 2 \times \pi r_p^2$, which replaces Eq. (A7) of U2016, which was given by $A_p = 4 \times \pi r_p^2$.

8. In formula 6 and 7 you have T_{CA}, e_s, s_i which seems undefined in the text (unless I miss them). I guess they are defined in U2016, but I think you should defined them here too.

Yes, you are right, thanks for noticing. Generally, we decided to change T_{amb} into T_{CA} to make it clearer that temperature is prescribed at cruise altitude in our setup. Therefore, we give the definition of T_{CA} already in Section 2.2:

Previous research has highlighted the importance of ambient temperature at cruise altitude T_{CA}, ambient relative humidity $RH_{i,amb}$, and atmospheric stratification N_{BV} (described by the Brunt-Väisälä frequency) as key input parameters.

Specifying e_s and s_i, we added the following into Section 3.3:

The water vapor saturation pressure is represented by e_s, and s_i=RH_i-1 denotes the supersaturation.

Review 2

Dear reviewer,

Thank you very much for your comments and your feedback. We hope that the new version adequately addresses the points you raised. Please find below how we tackled your comments.

General comments

This manuscript presents a numerical study of ice crystal formation behind hydrogen-powered aircraft using a 3D large-eddy simulation (LES) framework coupled with a Lagrangian microphysical model. The focus lies on the vortex phase of contrail evolution, with a comparative analysis between hydrogen- and kerosene-fueled aircraft. The study explores the sensitivity of contrail properties to ambient humidity, temperature, initial ice crystal properties, and aircraft type. A new parameterization for the survival fraction of ice crystals under hydrogen combustion scenarios is proposed and tested against the LES results.

This is a timely and relevant contribution, particularly given the increasing interest in low-emission aviation technologies. The manuscript is well written and the results are clearly presented. I believe this study is of high quality and should be published after addressing a few key issues. In particular, the mesh resolution near the vortex core appears coarse when compared to prior studies (e.g., http://dx.doi.org/10.1063/1.4807063, https://doi.org/10.1063/1.4934350), which used at least 10 grid points across the vortex core radius. I would encourage the authors to comment on this, and ideally to provide a resolution sensitivity test (e.g., for both A350 and A320 cases), particularly regarding contrail properties such as vertical profiles of ice mass and ice crystal survival fractions.

We greatly appreciate your comment. As stated earlier in this document and in response to a similar point raised by Reviewer 1, we repeated one of the baseline simulations using a finer mesh resolution. The outcome supports our conclusion that the originally used resolution is sufficient for the objectives of this study, which primarily focuses on hydrogen propulsion effects by varying the initial ice crystal number and water vapor emissions. The specific results and interpretation of the grid sensitivity analysis are provided in our response to Comment 2 of Reviewer 1 and detailed in Section 3 of the supplement.

Specific comments

1. Section 2.1 (second paragraph): The Lagrangian particle framework is introduced, but it is not stated whether drag forces acting on the particles are considered. Given that the ice crystals exceed 1 µm in radius, could the authors clarify whether drag is included in the particle dynamics?

   Thank you for this thoughtful comment. In the current framework, drag is not considered. The effect of particle inertia, specifically in terms of centrifugal acceleration, was investigated in Unterstrasser, 2014, JGR. That study found that inertial effects may become relevant for larger particles located at plume positions exposed to the maximum tangential velocity

induced by the rotating vortices. In these specific cases, particles may leave the vortex system due to inertial effects. However, we believe this phenomenon affects only the largest particles, which would, anyway, likely survive adiabatic heating. Therefore, we consider the impact on the survival fraction to be negligible. Additionally, it is important to note that ice crystals captured within the trailing vortices tend to shrink over time, making them less susceptible to centrifugal forces. Moreover, as the simulation progresses, the vortex circulation—and consequently the tangential velocity—decreases, further reducing the influence of inertial effects.
From a computational perspective, including inertial effects would require a significantly smaller time step—on the order of 10^{-5} seconds compared to the 10^{-2} seconds used in the current framework—leading to a substantial increase in computational cost for the computation of the particles' trajectories. Given the probably limited impact of inertia on the key metric of survival fraction and considering the additional computational expense, we believe its exclusion is justified in the context of this study.

We included the following sentence into Section 2.1:

The effect of particle inertia, specifically centrifugal acceleration in the rotating wake vortices, is neglected due to the small ice crystal sizes present in the primary wake, as shown in Unterstrasser, 2014, JGR.

2. Line 124: You mention the simulation starts "several seconds" after emission. Can you specify the exact time corresponding to the plume age? This is important for comparison with prior studies (e.g., https://doi.org/10.5194/acp-15-7369-2015).

   We acknowledge your interest in a precise specification of the initialization time and understand the intention to assess the comparability of initial conditions across different studies. However, we believe that providing a specific value is not particularly meaningful in this context. The focus of our analysis is analyzing contrail properties after vortex break-up, and model comparisons should focus on contrail properties at that time.

3. Line 121: Please clarify what is meant by "rigid boundary conditions". Do you refer to the vertical boundaries being reflective, fixed-value, or another type?

   Thank you for this comment. Rigid boundary conditions mean that any flux across the vertical boundaries in normal direction is prohibited. Along the boundary surface, free slip is assumed. As pointed out in our reply to Minor comment 3 of Reviewer 1, we included an additional description into Section 2.2.

4. Line 170: About the initial crystal distribution, I understand the lack of direct measurements of crystal properties (e.g., radius and density), but more explanation on how the initial mean radius and density were selected would be appreciated. Was this based on previous simulations (e.g., https://doi.org/10.5194/acp-24-2319-2024), theoretical estimates, or adjusted to match a specific ice number emission index?

   Thank you for your hint that we need to specify this. Our reply is a bit verbose, as we are not sure whether density refers to the density of ice or the mass/number concentrations of the ice crystal population.

   In our setup, the initial total contrail ice mass I_0 per unit length is given by the amount of emitted water vapor, and the analogous quantity for the number is denoted as N_0. I_0 and N_0

*are the main parameters that are varied in our study (besides temperature and aircraft type). From those two quantities, the mean ice crystal mass follows simply as I_0/N_0. The (geometric) mean radius can be computed with further assumptions on the ice crystal habit, density of ice, and shape of the size distribution. The initial mass and number concentrations simply follow from I_0/A_0 and N_0/A_0, where A_0 is the cross-sectional area of the initial plumes. Clearly, uniform plume concentrations are an idealization. Hence, the values of "*radius and density*" (we believe you refer to ice crystal mean mass and ice crystal mass/number concentration) are direct consequences of our setup parameters and choices.*

We added the following in Section 2.2:

For this estimate, we use a density of ice $\rho_i = 0.92\ gcm^{-3}$, and assume spherical particles, which is a reasonable approximation for small ice crystals with aspect ratios close to one. The radius corresponding to the mean particle mass, r_0, is then approximated by $\sim (I_0/(\rho_i N_0))^{1/3}$, assuming that all emitted water vapor is deposited onto the ice crystals. While the LCM represents ice crystal habits as hexagonal columns, this simplified estimate for r_0 serves as a first-order approximation to illustrate the general relationship between N_0, I_0, and the resulting crystal size.

Technical corrections

1. In lines 309, should be "A320 aircraft" not "A320aircraft".
2. In lines 309, should be "with a wing span" not "with wing span".

Thank you very much for the careful reading of the manuscript. We corrected the oversights.

High-resolution modelling of early contrail evolution from hydrogen-powered aircraft

Annemarie Lottermoser and Simon Unterstrasser
Deutsches Zentrum für Luft- und Raumfahrt, Institut für Physik der Atmosphäre, Oberpfaffenhofen, Germany
Correspondence: Annemarie Lottermoser (annemarie.lottermoser@dlr.de)

Abstract. In this study, we investigate the properties of young contrails formed behind hydrogen-powered aircraft, particularly compared to contrails from conventional kerosene combustion. High-resolution simulations of individual contrails are performed using the EULAG-LCM model, a large-eddy simulation model with fully coupled particle-based ice microphysics.

Previous studies on early contrail evolution during the vortex phase explored a range of meteorological and aircraft-related parameters but focused on contrails with ice crystal numbers and water vapor emissions typical of kerosene combustion.

This study examines the early H_2-contrail evolution, starting tenths of a second after exhaust emission when ice crystal formation is complete. Two key parameters are adjusted: the ~~amount of~~ emitted water vapor mass and the number of ice crystals formed during the initial stage. The emitted water vapor varies between 3.7 and 38.6 g per flight meter, depending on the fuel and aircraft type. The initial ice crystal number spans four orders of magnitude, from approximately 10^{10} to 10^{14} ice crystals per flight meter. Additionally, we extend our atmospheric scenarios to ambient temperatures up to 235 K, as H_2 contrails can form in warmer conditions where kerosene plumes typically cannot.

Our results show that vortex phase processes reduce the four-order magnitude difference in ice crystal number to two orders of magnitude. Moreover, relative ice crystal loss increases with increasing ambient temperatures and decreasing relative humidity levels.

Finally, we extend the parametrization of ice crystal loss from a previous study to include scenarios of contrails from hydrogen propulsion systems.

1 Introduction

For conventional kerosene-powered aircraft, the primary exhaust emissions consist of carbon dioxide and water vapor, with approximately 1.26 kg of water vapor emitted per kilogram of fuel burned (Bier et al., 2024). If the ambient atmosphere is sufficiently cold, water supersaturation emerges due to the mixing of the hot exhaust gases with the cold ambient air (Schumann, 1996). This happens within tenths of a second after the emission of the exhaust. Under these conditions and in the case of soot-rich combustion, water vapor condenses onto soot particles in the exhaust, forming water droplets that grow and eventually freeze into contrail ice crystals by homogeneous nucleation (Kärcher et al., 2015). In ice-supersaturated conditions, these young (i.e. several minutes old) line-shaped contrails can evolve into ~~contrail cirrus~~contrail-cirrus, which may persist for several hours (Lewellen et al., 2014; Unterstrasser et al., 2017a). ~~Contrail cirrus~~ Contrail-cirrus has been identified as a significant contributor

to aviation-induced radiative forcing. On a global scale, contrail-cirrus exert a positive radiative forcing, resulting in a net warming effect on the atmosphere (Burkhardt and Kärcher, 2011; Lee et al., 2021; Bier and Burkhardt, 2022).

Several contrail mitigation strategies are currently under debate, and their mitigation potential is estimated. Adaptations of flight routes can pursue avoiding ice-supersaturated regions, where contrail formation and persistence are likely to happen (Gierens et al., 2020; Lee et al., 2023). Flying in formation reduces the contrail climate impact due to saturation effects (Marks et al., 2021; Unterstrasser, 2020). Moreover, modifying the fuel composition (e.g. by using sustainable aviation fuels (SAFs)) can reduce the number of emitted soot particles (Moore et al., 2017). Measurements have demonstrated that using alternative fuel blends can reduce the number of ice crystals formed as the contrail ice crystals primarily form on the emitted exhaust particles (Bräuer et al., 2021; Voigt et al., 2021). Märkl et al. (2024) find, in the specific case of the ECLIF3 experiment, a 56 % reduction in ice particle number per mass of burnt fuel for 100 % SAF compared to a reference Jet A-1 fuel. The initial ice crystal number is the crucial quantity that controls the contrail radiative effect and life cycle for given meteorological conditions (Unterstrasser and Gierens, 2010; Burkhardt et al., 2018). A systematic reduction of the ice crystal number in ~~contrail cirrus~~contrail-cirrus, e.g. triggered by using SAFs, decreases their optical depth and, consequently, their global radiative forcing (Bier et al., 2017; Burkhardt et al., 2018). However, Burkhardt et al. (2018) have found that the relationship between ice crystal number in young contrails and the climate impact of ~~contrail cirrus is non-linear~~contrail-cirrus is nonlinear. Consequently, recent advancements are being explored to reduce the number of emitted particles even further, such as transitioning to hydrogen-powered aircraft. As part of the ZEROe project, Airbus plans to build the first commercial hydrogen-powered aircraft by 2035 (Airbus, 2020).

Hydrogen combustion results in exhaust plumes that are significantly moister than kerosene plumes (containing approximately ~~seven~~ 2.6 times more water vapor), and entrained atmospheric background aerosol particles are expected to serve as contrail ice nuclei, as hydrogen exhaust plumes are void of soot particles (Kärcher et al., 2015; Bier et al., 2024). Recent research by Bier et al. (2024) indicates that hydrogen-powered aircraft could reduce the number of ice crystals formed in contrails by more than 80-90 % compared to kerosene contrails. While no soot particles are produced during hydrogen combustion, the formation of ultrafine volatile particles is possible (Ungeheuer et al., 2022), and their role in ice crystal formation is not yet understood.

Another technological option using hydrogen as an energy carrier employs a hydrogen fuel cell propulsion system (also proposed in the ZEROe project). Hydrogen fuel cells create electrical energy that turns a propeller or fan. Fuel cells offer several advantages over conventional combustion-based technologies as they are expected to operate at a higher overall propulsion efficiency (Kazula et al., 2023). Moreover, hydrogen fuel cells eliminate emissions of carbon dioxide and nitrogen oxides. Despite ongoing development efforts, several uncertainties regarding the performance and operation of fuel cell propulsion systems remain, making this an active field of research. According to the contrail formation theory for fuel cells (Gierens, 2021), the supersaturation over water in the exhaust plume of such systems could be significantly higher than for conventional combustion systems. This leads to a much larger slope of the mixing line as described by the Schmidt-Appleman theory (Schumann, 1996), which defines the linear relationship between plume partial water vapor pressure and temperature. The plume supersaturation can attain very high values, which could trigger homogeneous droplet nucleation (HDN; Wölk and

Strey, 2001) and the formation of numerous small water droplets (Jansen and Heymsfield, 2015). Given the low ambient temperatures at typical cruise altitudes, these droplets would rapidly freeze, potentially resulting in a very high initial number of ice crystals. In this study, we address the potential implications of this propulsion system by artificially increasing the initial number of ice crystals in our simulations. We emphasize that we do not state that fuel cell propulsion leads to a high number of contrail ice crystals. Moreover, there are design options under consideration that may avoid abundant ice crystal production. Hence, our scenarios with high ice crystal numbers should be interpreted just as one possible scenario of fuel cell propulsion.

The initial properties of contrails, such as the number of ice crystals, are crucial for evaluating the radiative properties of ~~contrail cirrus~~contrail-cirrus. For a thorough assessment of contrail mitigation options that aim to reduce the number of ice crystals during the initial formation stage, it is essential to examine the implications of the formation processes and consider the subsequent evolution of the contrail during the vortex phase. The vortex phase covers the first few minutes in the contrail's lifetime. The primary process is the interaction of the contrail ice crystals with the descending counter-rotating vortex pair. This consideration is necessary because the initial contrail ice crystal number closely matches the emitted soot particle number only under low temperature and high supersaturation conditions (Bier and Burkhardt, 2022). In contrast, significant deviations can occur under weakly supersaturated conditions and high ambient temperatures. Adiabatic heating in the descending vortex pair increases the saturation pressure, lowering the plume relative humidity. This may lead to the sublimation of the ice crystals trapped in the descending vortices (Lewellen and Lewellen, 2001; Unterstrasser and Sölch, 2010). The survival fraction of ice crystals after the vortex phase is highly influenced by factors such as the number of nucleated ice crystals, the amount of emitted water vapor, ambient temperature, relative humidity over ice, Brunt-Väisälä frequency, and the aircraft's wingspan. Generally, the fraction of ice crystals lost during the vortex phase is larger/smaller, the more/fewer ice crystals are present in the beginning. The initial number of ice crystals is related to the aircraft's fuel flow rate and an assumed apparent ice crystal emission index EI_{iceno} (Unterstrasser and Sölch, 2010; Lewellen et al., 2014). Unterstrasser (2016) states that an initial reduction of EI_{iceno} from 10^{15} to $10^{14}\,kg^{-1}$ implies only a factor 5.3 reduction of the ice crystal number after the vortex phase. Hence, initial differences in the ice crystal number (e.g. by changes in the fuel or engine/combustor design) are reduced during the vortex phase. This means that a decreased ice crystal loss in the vortex phase partly compensates for the reduced ice nucleation (Bier and Burkhardt, 2022). The consideration of ice crystal loss processes during the vortex phase, as parametrized in Unterstrasser (2016) and implemented in larger scale models, lead to significant changes in the later contrail properties on regional (Gruber et al., 2018) and global scale (Bier and Burkhardt, 2022).

In this study, we systematically investigate the properties of young H_2 contrails with a focus on various ambient and meteorological parameters. In Sec. 2, we present the model and the parameter setup. Section 3 focuses on the sensitivity of H_2 contrails to various parameters. Also, we present the updated parametrization in this section. Implications of the simulation results are discussed in Sec. 4, and conclusions are drawn in Sec. 5.

2 Methods

In this section, we introduce our model (Sec. 2.1) and describe the numerical setup employed in our simulations (Sec. 2.2). Furthermore, we define the specific quantities necessary for evaluating and analyzing the results (Sec. 2.3).

2.1 Model

We perform simulations of H_2 contrails using the LES model EULAG-LCM. The base LES code EULAG solves the anelastic formulation of the momentum and energy equations (Smolarkiewicz and Margolin, 1997; Prusa et al., 2008). The microphysical module LCM, which incorporates a Lagrangian particle-tracking method, has been coupled to EULAG (Sölch and Kärcher, 2010), resulting in the model version EULAG-LCM. This model version has been used in multiple previous studies to explore the properties of young contrails during the vortex phase (e.g. Unterstrasser and Sölch, 2010; Unterstrasser, 2014; Unterstrasser and Stephan, 2020) and their transition into contrail-cirrus (Unterstrasser et al., 2017a, b; Unterstrasser, 2020). The model results have also been used to develop a parametrization of ice crystal loss and the geometric depth of contrails after vortex break-up (Unterstrasser, 2016).

In the particle-based framework of LCM, ice crystals are represented by simulation particles. Each simulation particle (SIP) represents a certain number of real ice crystals (referred to as the weight of the SIP) with identical properties, such as size and mass. The effect of particle inertia, specifically centrifugal acceleration in the rotating wake vortices, is neglected due to the small ice crystal sizes present in the primary wake, as shown in Unterstrasser (2014).

In this study, we consider the deposition growth and sublimation of ice crystals and latent heat release to be the most important microphysical processes and switch off several LCM routines, such as aggregation and radiation.

2.2 Numerical setup and set of simulations

Generally, we assume ambient conditions such that contrails form and persist, i.e. the atmosphere is sufficiently cold and moist (Schumann, 1996; Gierens and Spichtinger, 2000).

As hydrogen propulsion technology is likely to be initially employed on smaller aircraft, we conduct simulations for both an aircraft with a wing span of 60.3 m (A350/B777-like aircraft, default) and a smaller aircraft with a wing span of 34.4 m (A320/B737-like aircraft). Generally, the setups are consistent with a previous EULAG-LCM study, where contrails from six different aircraft types were systematically investigated (Unterstrasser and Görsch, 2014). Throughout the text, when we use "A350" ("A320") aircraft, we are specifically referring to an "A350/B777-like" aircraft ("A320/B737-like" aircraft).

The ~~numbers~~ number of grid points in our default model domain ~~are~~ is $n_x = 384$, $n_y = 200$, and $n_z = 600$, where x, y, and z denote the transverse, longitudinal (along flight direction), and vertical direction, respectively. The size of the simulation domain ~~depends, e. g., on stratification: A~~ is adjusted based on specific conditions. For example, weaker stratification requires a larger ~~simulation domain~~domain, as the vortices descend further ~~downwards. Moreover, the vortices exhibit a greater meandering because~~ and exhibit more pronounced meandering due to the Crow instability ~~is more pronounced (Crow, 1970) .~~ (Crow, 1970). Additionally, for high cruise-altitude temperatures (i.e. $T_{CA} = 230$, 233, and 235 K), the vertical domain size

was increased from 600 to 800 grid points for the A350, and from 856 to 1112 grid points for the A320. The grid resolution is 1 m along the transverse and vertical and 2 m along the longitudinal direction. For simulating an A320 aircraft, the resolution is changed to $\mathrm{d}x = \mathrm{d}z = 0.57\,\mathrm{m}$ and $\mathrm{d}y = 1.14\,\mathrm{m}$ as described in Unterstrasser and Görsch (2014). For both aircraft types, the domain size in flight direction is chosen to allow the formation of the most unstable Crow mode. Periodic boundary conditions are applied in the horizontal and longitudinal directions~~, while~~ . In the vertical direction, rigid boundary conditions are used~~in the vertical direction~~, meaning that the vertical velocity component is zero at the top and bottom boundaries of the simulation domain. The total simulated time is around six to seven minutes, where the time step increases from initially 0.03 s to 0.08 s at later stages of the simulation.

The simulations start at a plume age of several seconds. At this stage, it can be assumed that the ice crystal formation is finished and the vortices have fully rolled up. We initialize the ice crystals in two discs (one per wing) with uniform ice crystal number concentrations. The flow field is a superposition of a turbulent background field and two counter-rotating Lamb-Oseen vortices. The vortex circulation, vortex core radius, and plume radius depend on the aircraft type and are given in Tab. 1.

We incorporate the effects of a hydrogen propulsion system by varying the initial number of ice crystals N_0 and the ~~initial amount of~~ emitted water vapor mass I_0. The default values of the initial ice crystal number correspond to typical values of the fuel flow rate, denoted by $\dot{m}_\mathrm{F}$~~(as reported in Unterstrasser and Görsch (2014))~~, and an apparent ice emission index $\mathrm{EI}_\mathrm{iceno} = 2.8\times10^{14}\,\mathrm{kg}^{-1}$ (Unterstrasser and Görsch, 2014), which represents a typical kerosene contrail. N_0 is then determined by

$$N_0 = m_\mathrm{C} \times \mathrm{EI}_\mathrm{iceno}, \tag{1}$$

where the fuel consumption m_C is defined as $m_\mathrm{C} := \dot{m}_\mathrm{F}/U_\infty$. U_∞ represents the aircraft velocity~~, and $\dot{m}_\mathrm{F}$ denotes the fuel flow rate~~. The reference values are $N_{0,\mathrm{ref}} = 0.85 \times 10^{12}\,\mathrm{m}^{-1}$ for an A320 aircraft and $3.38 \times 10^{12}\,\mathrm{m}^{-1}$ for an A350 aircraft.

To explore a broad range of scenarios, we scale N_0 up and down by factors of 10 and 100 relative to $N_{0,\mathrm{ref}}$. The downscaling simulations are supposed to cover hydrogen combustion scenarios. Conversely, the upscaling simulations could represent scenarios involving a hydrogen fuel cell propulsion system with HDN occurring (see Sec. 1). Varying the number of ice crystals in the model is achieved by varying the weight of the SIPs, which keeps their total number roughly the same. Clearly, the assumptions on the initial ice crystal number are made for hypothetical aircraft designs, and the research on contrail formation processes in H_2 plumes started only recently (Bier et al., 2024; Ponsonby et al., 2024). A more in-depth discussion of the representativity of our N_0 choice is deferred to Sec. 4.

Analogously to N_0, the ~~emission of water vapor~~ emitted water vapor mass is calculated using

$$I_0 = m_\mathrm{C} \times \mathrm{EI}_{\mathrm{H_2O}}, \tag{2}$$

where $\mathrm{EI}_{\mathrm{H_2O}}$ is the emission index of water vapor, with a value of $1.26\,\mathrm{kg\,kg}^{-1}$ for all aircraft types ~~(Unterstrasser and Görsch, 2014)~~ (Bier et al., 2024). We increase I_0 by multiplying the default values, $3.7\,\mathrm{g\,m}^{-1}$ for an A320 aircraft and $15.0\,\mathrm{g\,m}^{-1}$ for an A350 aircraft (referred to as $I_{0,\mathrm{kero}}$), with 2.57 resulting in $9.51\,\mathrm{g\,m}^{-1}$ and $38.55\,\mathrm{g\,m}^{-1}$ (referred to as $I_{0,\mathrm{H_2}}$), respectively. The value of 2.57 corresponds to the ratio of the emission index of water vapor divided by the combustion heat Q of hydrogen to kerosene

(Bier et al., 2024). Note that N_0 and I_0 are given in units "per meter of flight path". Table 2 summarizes the key differences between hydrogen and kerosene fuel and exhaust properties.

We want to mention one caveat that is crucial for properly interpreting the comparison between the H_2 and kerosene scenarios. According to Tab. 2, switching from kerosene to H_2, the water vapor emission index increases by a factor 7.1, while the specific heat of combustion is higher by a factor of 2.79. The energy-specific water emission is then 2.57 times higher, which is, by the way, a crucial difference affecting the contrail formation process and potential contrail coverage (Schumann, 1996; Bier et al., 2024; Kaufmann et al., 2024). Achieving the same work rate with both fuel types, the hydrogen fuel consumption is 2.79 times lower, and the water vapor emission (per flight distance) I_0 is 2.57 times larger. Moreover, it is our design choice to assume the same $N_{0,\mathrm{ref}}$ value for both fuel scenarios. This implies that the reference apparent ice emission index $\mathrm{EI}_{\mathrm{iceno,ref}}$ of the H_2 scenarios (i.e. those simulations with higher I_0 values) is actually larger by a factor of 2.79. Comparing a factor "100 down" simulation with larger I_0 values (as a typical representative of a H_2 contrail) with a conventional kerosene contrail (i.e. reference N_0 and smaller I_0 values), must not be interpreted as a factor-100 variation of $\mathrm{EI}_{\mathrm{iceno,ref}}$. The difference is actually smaller (factor ~ 36).

Following e.g. Unterstrasser and Sölch (2010), the initial ice crystal size distribution is represented by a lognormal distribution with a width parameter r_{SD}. We adopt a default value of $r_{\mathrm{SD}} = 3.0$ and explore variations with a narrower ($r_{\mathrm{SD}} = 1.0$, monodisperse) and broader ($r_{\mathrm{SD}} = 4.0$) initial size distribution, as previous studies have identified this parameter as significant (Unterstrasser and Sölch, 2010; Unterstrasser, 2014). Note that other modelling studies that initialize the contrails at an earlier state without the specification that all emitted water vapor has already been deposited on the ice crystals show a weaker impact of the width parameter (Lewellen et al., 2014). We conducted simulations only with a 100-fold increase or decrease when altering the width parameter (to reduce the number of simulations).

Figure 1 shows the mean ice crystal radius versus the initial number of ice crystals for kerosene and hydrogen water vapor emission. For this estimate, we use a density of ice, $\rho_{\mathrm{i}} = 0.92\,\mathrm{g\,cm^{-3}}$, and assume spherical particles, which is a reasonable approximation for small ice crystals with aspect ratios close to one. The radius corresponding to the mean particle mass, r_0, is then approximated by $\sim \left(\frac{I_0}{\rho_{\mathrm{i}} N_0}\right)^{1/3}$, assuming that all emitted water vapor is deposited onto the ice crystals. While the LCM represents ice crystal habits as hexagonal columns, this simplified estimate for r_0 serves as a first-order approximation to illustrate the general relationship between N_0, I_0, and the resulting crystal size. A higher N_0 value generally results in a smaller mean radius because the total amount of water is distributed among more particles~~, causing each particle to receive less water~~. It is also evident that the initial water content I_0 directly affects the initial particle size: ~~The~~ the higher I_0 (indicated by triangles that represent the hydrogen case), the larger the initial particles. The initial mean ice crystal radii remain unaffected by a variation in the initial width of the size distribution r_{SD}.

Additionally, we investigate the influence of different atmospheric conditions on the evolution of contrail ice crystals. ~~At the lower boundary of the simulation domain, the pressure is $250\,\mathrm{hPa}$ and the air density is roughly $0.4\,\mathrm{kg\,m^{-3}}$ changing with the prescribed ambient temperature. We use a background turbulence field with an eddy dissipation rate $\epsilon = 10^{-7}\,\mathrm{m^2\,s^{-3}}$.~~ Previous research has highlighted the importance of ambient temperature at cruise altitude T_{CA}, ambient relative humidity with respect to ice $RH_{\mathrm{i,amb}}$, and atmospheric stratification N_{BV} (described by the Brunt-Väisälä frequency) as key input parameters (Lewellen

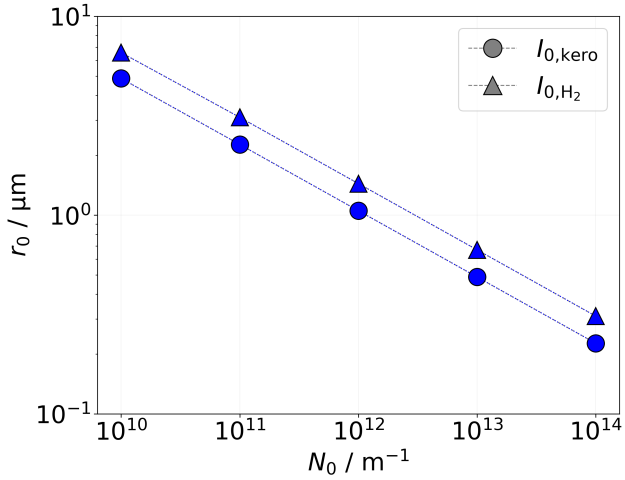

Figure 1. Mean initial ice crystal radius as a function of the initial number of ice crystals. Its sensitivity regarding the microphysical initialization in terms of I_0 (symbol) is depicted.

et al., 2014; Unterstrasser, 2016). We vary these parameters as outlined in Tab. 1. ~~Values~~ At the lower boundary of the simulation domain, we prescribe an air pressure of $p_0 = 250\,\mathrm{hPa}$ and an air density of approximately $\rho_{\mathrm{air},0} = 0.4\,\mathrm{kg\,m^{-3}}$. For ambient temperature, we prescribe cruise-altitude values of $T_{\mathrm{CA}} = 217$, 225, 230, 233, and 235 K. The relative humidity with respect to ice is assumed to be constant throughout the entire simulation domain and set to either 110 or 120 %. We use a background turbulence field with an eddy dissipation rate of $\epsilon = 10^{-7}\,\mathrm{m^2\,s^{-3}}$. The pressure and temperature vertical profiles are computed for an atmosphere with a vertically constant Brunt-Väisälä frequency according to Eq. 2 in Clark and Farley (1984). At cruise altitude, the resulting air pressure ranges from 231 to 235 hPa, depending on Brunt-Väisälä frequency and temperature. In Tab. 1, an average air pressure value is provided. It would seem appropriate to vary ambient pressure in combination with T_{CA} to reflect a change in flight altitude. However, a variation of pressure has only little impact on the simulated contrail properties as demonstrated in Sec. 3.3 in the supplement. This is because the background water vapor mass concentration is independent of ambient pressure. Hence, we do not adapt p_0.

In Tab. 1, values that are marked with a star refer to the default simulation of an A350 aircraft with a water vapor emission that corresponds to a kerosene combustion system $I_0 = 15.0\,\mathrm{g\,m^{-1}}$ and initial ice crystal number $N_0 = 3.38 \times 10^{12}\,\mathrm{m^{-1}}$ at ambient temperature of 217 K, ambient relative humidity with respect to ice of 120 %, and a standard value for atmospheric stability of $1.15 \times 10^{-2}\,\mathrm{s^{-1}}$. Ice crystal formation is improbable for ambient temperatures exceeding 233 K, as this surpasses the homogeneous freezing temperature (Bier et al., 2024), and liquid droplets that form first in the cooling exhaust plume would not freeze. Nevertheless, we include simulations with ambient temperatures of 233 K and 235 K as limiting cases, as droplet freezing in turbulent and quickly cooling plumes is not well-constrained. An overview of all performed simulations is provided in Tab. A1.

Aircraft and vortex parameters			Ice crystal parameters		
	A320/B737	A350/B777*		A320/B737	A350/B777
b_{span} / m	34.4	60.3	N_0 / ($[10^{10}, 10^{11}, 10^{12*}, 10^{13}, 10^{14}]\,\text{m}^{-1}$)	0.85	3.38
Γ_0 / ($\text{m}^2\,\text{s}^{-1}$)	240	520	I_0 / ($10^{-3}\,\text{kg}\,\text{m}^{-1}$)	[3.7*, 9.51]	[15.0*, 38.55]
r_c / m	3.0	4.0	r_{SD}	[1.0, 3.0*, 4.0]	
r_{plume} / m	12	20			
Atmospheric conditions			Numerical parameters		
~~p_{air} / ($\text{kg}\,\text{m}^{-3}$)~~ $\rho_{\text{air,CA}}$ / ($\text{kg}\,\text{m}^{-3}$)	0.36			A320/B737	A350/B777
~~p_{amb} / (10^2 Pa)~~ p_{CA} / (10^2 Pa)	233		$\text{d}x, \text{d}y, \text{d}z$ / m	0.57, 1.14, 0.57	1, 2, 1
~~T_{amb} / K~~ T_{CA} / K	[217*, 225, 230, 233, 235]		n_x, n_y, n_z	384-768, 200, 600-1112	
$RH_{\text{i,amb}}$ / %	[110, 120*]		t_{sim} / s	≈ 400	
ϵ / ($\text{m}^2\,\text{s}^{-3}$)	10^{-7}		$\text{d}t$ / s	0.03 - 0.08	
N_{BV} / ($10^{-2}\,\text{s}^{-1}$)	[0.5, 1.15*]				

Table 1. Aircraft/vortex, ice crystal, atmospheric, and numerical parameters. Multiple values in square brackets refer to sensitivity studies, and values with a star refer to default values. b_{span}: wingspan; Γ_0: circulation; r_c: vortex core radius; r_{plume}: plume radius at initialization; N_0: initial number of ice crystals; I_0: ~~initial amount of~~ emitted water vapor mass; r_{SD}: width of initial ice crystal size distribution; ~~p_{air}~~ $\rho_{\text{air,CA}}$: air density at cruise altitude; ~~p_{amb}~~ p_{CA}: ~~ambient~~ air pressure at cruise altitude; ~~T_{amb}~~ T_{CA}: ambient temperature at cruise altitude; $RH_{\text{i,amb}}$: ambient relative humidity with respect to ice; ϵ: eddy dissipation rate; N_{BV}: Brunt-Väisälä frequency; $\text{d}x, \text{d}y, \text{d}z$: mesh sizes; n_x, n_y, n_z: number of grid points; t_{sim}: simulated time; $\text{d}t$: time step.

2.3 Quantities of interest

In the following, we give definitions of quantities that are used throughout the paper.

The total number of ice crystals per meter of flight path and the vertical ice crystal number profile are defined as

$$N_{\text{tot}}(t) = \frac{1}{L_y} \int\int\int \iiint N(x,y,z,t)\,\text{d}x\,\text{d}y\,\text{d}z \quad \text{and} \tag{3}$$

$$N_{\text{v}}(z,t) = \frac{1}{L_y} \int\int \iint N(x,y,z,t)\,\text{d}x\,\text{d}y. \tag{4}$$

Both quantities are averaged along flight direction. The total ice mass M_{tot} and the vertical ice mass profile M_{v} are computed analogously. The normalized ice crystal number is calculated as

$$f_N(t) = \frac{N_{\text{tot}}(t)}{N_0}. \tag{5}$$

In Sec. 3, we will use the term "survival fraction of ice crystals" $f_{N,\text{s}}$, which is the normalized ice crystal number at the end of the simulation. Another pertinent quantity to examine is the number of sublimated ice crystals N_{subl}. Vertical normalized

fuel/exhaust parameters	hydrogen	kerosene	ratio
$\mathrm{EI_{H_2O}}\,/\,(\mathrm{kg\,kg^{-1}})$	**8.94**	1.26	7.10
$Q\,/\,(10^6\,\mathrm{J\,kg^{-1}})$	**120**	43	2.79
$\mathrm{EI_{H_2O}}\,Q^{-1}\,/\,(10^{-6}\,\mathrm{kg\,J^{-1}})$	**0.075**	0.029	2.57
	A320/B737		
$m_\mathrm{C}\,/\,(10^{-3}\,\mathrm{kg\,m^{-1}})$	1.06	2.96	2.79^{-1}
$I_0\,/\,(10^{-3}\,\mathrm{kg\,m^{-1}})$	9.51	3.7	2.57
$N_\mathrm{0,ref}\,/\,(10^{12}\,\mathrm{m^{-1}})$	0.85	0.85	1
$\mathrm{EI_{iceno,ref}}\,/\,(10^{14}\,\mathrm{kg^{-1}})$	7.81	2.8	2.79
	A350/B777		
$m_\mathrm{C}\,/\,(10^{-3}\,\mathrm{kg\,m^{-1}})$	4.3	12.0	2.79^{-1}
$I_0\,/\,(10^{-3}\,\mathrm{kg\,m^{-1}})$	38.55	15.0	2.57
$N_\mathrm{0,ref}\,/\,(10^{12}\,\mathrm{m^{-1}})$	3.38	3.38	1
$\mathrm{EI_{iceno,ref}}\,/\,(10^{14}\,\mathrm{kg^{-1}})$	7.81	2.8	2.79

Table 2. Fuel, engine, and exhaust parameters for hydrogen propulsion (second column), kerosene (third column) and the ratio between both (fourth column). The water vapor mass emission index and specific heat of combustion ("lower calorific value") are based on Tab. 1 of Schumann (1996).

profiles $f_{N,\mathrm{v,subl}}$ are computed as described in Eqs. 3-5 and track the number of ice crystals that ~~sublimated~~ sublimate at a specific altitude.

3 Results

3.1 Exploring H_2 contrails

In this section, we examine the impact of the initial number of ice crystals and the ~~initial amount of water vapor~~ emitted water vapor mass, corresponding to an H_2 combustion engine or a potential fuel cell setup. These two parameters are varied as described in Sec. 2.2. The simulations presented in this section are performed for an A350 aircraft at ~~$T_\mathrm{amb} = 217\,\mathrm{K}$~~ $T_\mathrm{CA} = 217\,\mathrm{K}$, $RH_\mathrm{i,amb} = 120\,\%$, and $N_\mathrm{BV} = 1.15 \times 10^{-2}\,\mathrm{s^{-1}}$, which were also the baseline meteorological conditions in previous EULAG-LCM studies. Hence, this scenario is well-explored and the new simulations build upon the existing ones. Unless stated otherwise, the presented results use the default initial values (indicated by a star in Tab. 1).

Figure 2 (top row) illustrates the temporal evolution of contrail ice crystals in the x,z-plane over a six-minute period. The ice crystal number concentration is averaged along the flight direction. At the start of the simulation, two circular plumes are initialized at $z = 0\,\mathrm{m}$. The centers of the plumes and of the wake vortices are collocated on each side. Within the first

two minutes, a downward motion of the ice crystals is observed as the aircraft exhaust descends with the downward moving vortices, forming the primary wake. Also, we see a horizontal broadening of the contrail after few minutes due to the Crow instability (Crow, 1970). Ice crystals that are continuously detrained from the descending exhaust form a curtain between the original emission altitude and the vortex location, known as the secondary wake (Sussmann and Gierens, 1999; Unterstrasser, 2014). After six minutes, ice crystals are visible close to or even above the cruise altitude as the vertically displaced air masses rise back due to buoyancy after vortex ~~break up~~break-up. Whereas ice crystals in the secondary wake grow in size due to the deposition of the available water vapor, a significant portion of the ice crystals can sublimate in the primary wake because of adiabatic heating (Sussmann and Gierens, 1999; Lewellen and Lewellen, 1996; Unterstrasser, 2016).

The second row in Fig. 2 shows the cross-sectional ice crystal number concentrations after six minutes for the reference N_0-case ($N_0 = 3.38 \times 10^{12}\,\mathrm{m}^{-1}$) and the N_0-upscaling and N_0-downscaling cases. Higher final number concentrations in absolute terms are evident in the upscaling cases ($N_0 = 3.38 \times 10^{13}\,\mathrm{m}^{-1}$ and $N_0 = 3.38 \times 10^{14}\,\mathrm{m}^{-1}$). Nonetheless, relative to the initial number, fewer ice crystals survive in these cases, as illustrated in the third row, where the final vertical profiles of normalized ice crystal numbers (green curves) are depicted. This observation is further supported by the final vertical profiles of normalized sublimated ice ~~crystals~~ crystal numbers (orange curves). In the upscaling cases, ice crystals begin to sublimate at higher altitudes because they are smaller in size (see Fig. 1); a phenomenon that has already been described by Huebsch and Lewellen (2006) and Unterstrasser (2014).

Figures 3(a) and (b) display the temporal evolution of the normalized total ice crystal number and absolute total ice mass for different N_0- and I_0-values. The most significant reductions in f_N occur in the upscaling scenarios (red curves in Fig. 3(a)), while the N_0-downscaling simulations (blue curves) show little to no reduction in the temporal evolution of f_N. Due to a higher absolute number of surviving ice crystals in the upscaling cases, these scenarios also exhibit a larger final total ice mass (red curves lie above the blue ones in Fig. 3(b)). The greater loss of ice crystals in the upscaling scenarios is reflected in the survival fraction depicted in Fig. 3(c). Conversely, contrails with a lower value of N_0 (and thus larger initial crystals) are less prone to sublimation, resulting in a higher survival fraction. This implies that initial differences in ice crystal ~~numbers~~ number diminish over time. In this specific scenario, initial differences spanning four orders of magnitude (with N_0-scaling factors of 0.01 and 100) reduce to just two orders of magnitude (0.015 and 7.5) after the vortex phase. Moreover, initializing with a greater amount of emitted water vapor (indicated by circles in Fig. 3(c)) results in larger ice crystal sizes (refer to Fig. 1), which in turn increases the survival fraction and ice mass. In the $I_{0,\mathrm{H_2}}$ simulations, the reduction in initial differences is less pronounced, with the four orders of magnitude difference reducing to three orders by the end of the vortex phase.

3.2 Parameter study of H_2-contrail properties

3.2.1 Sensitivity to ambient conditions

As revealed in previous studies, the evolution of contrail ice crystal number and ice mass is highly sensitive to ambient conditions (Lewellen and Lewellen, 2001; Unterstrasser, 2016). This section investigates the impact of ambient relative humidity, temperature, and atmospheric stratification on H_2-contrail properties. Note that we performed simulations at ~~$T_{\mathrm{amb}} \geq 230\,\mathrm{K}$~~

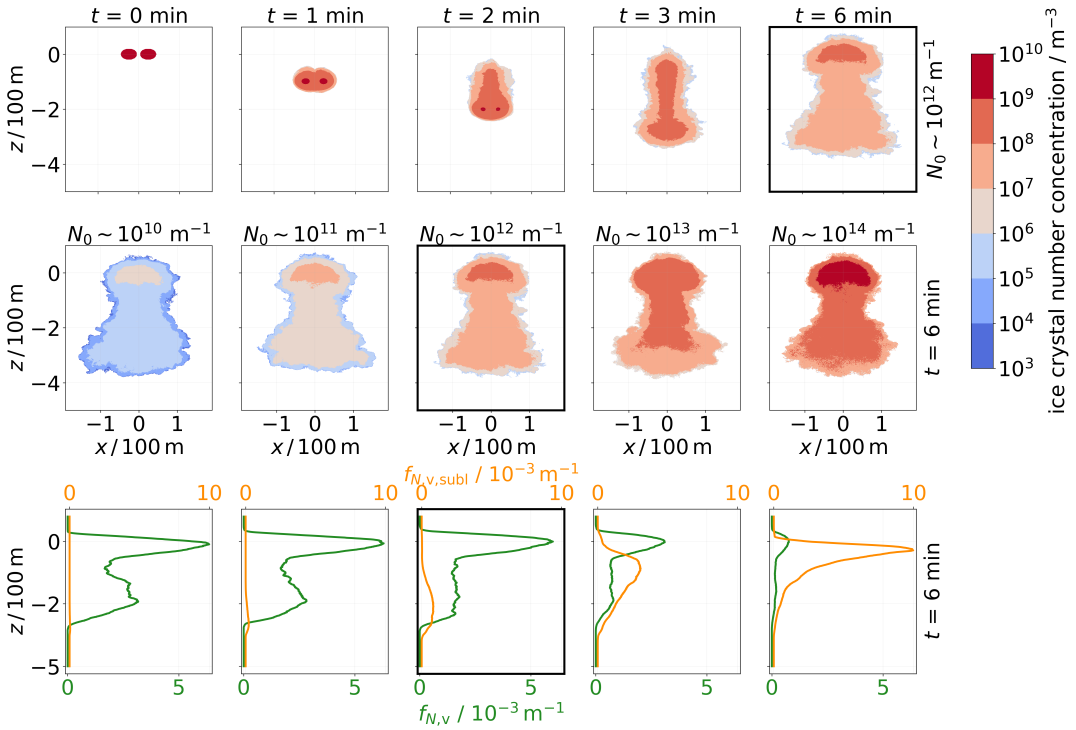

Figure 2. Ice crystal number concentrations, averaged along the flight direction in the x, z-plane, are depicted in the first and second rows. The first row illustrates the temporal evolution over six minutes. The final concentration distribution is displayed in the second row for five different N_0 values. The third row shows the normalized vertical profiles of ice crystals (green) and sublimated ice crystals (orange) (the first row depicts one simulation, and the second and third rows depict five different simulations). The simulation displayed in the top row refers to the simulation in the middle panels in the second and third rows, marked by the black frame. The displayed simulations are performed for an A350 aircraft at ~~$T_{\mathrm{amb}} = 217\,\mathrm{K}$~~ $T_{\mathrm{CA}} = 217\,\mathrm{K}$, $RH_{\mathrm{i,amb}} = 120\,\%$, and $I_0 = I_{0,\mathrm{H_2}}$. The z-coordinate is shifted such that $z = 0\,\mathrm{m}$ corresponds to the cruise altitude (which is also done in Figs. 4, 5, and 6).

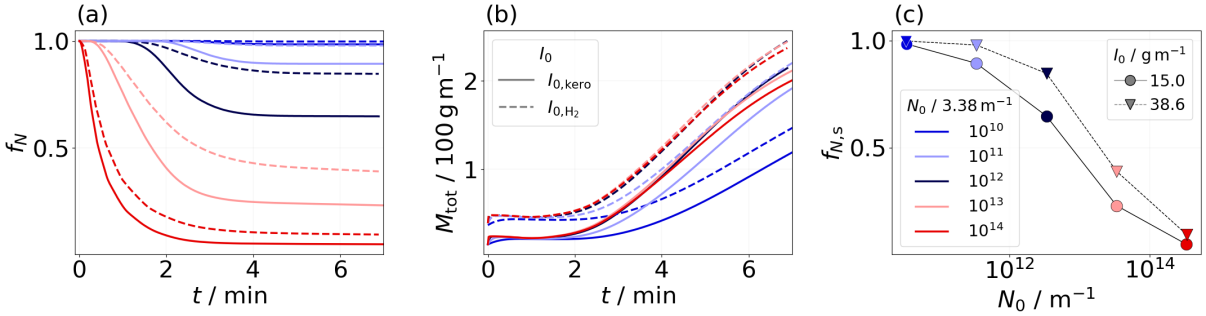

Figure 3. Temporal evolution of the normalized total number of ice crystals and total ice mass for different values of N_0 and I_0 ((a) and (b)). In panel (c), the survival fractions as functions of N_0 are depicted.

$T_{CA} \geq 230\,K$ only for H_2 contrails with an increased I_0 value as the formation of kerosene contrails is unlikely at these high ambient temperatures. The results presented in this section refer to simulations of an A350 aircraft with an initial size distribution width of $r_{SD} = 3.0$.

In Fig. 4, final vertical profiles of the ice crystal mass and normalized number and survival fractions (after approximately six minutes) are depicted. Columns represent simulations at temperatures of 217 K, 225 K, 230 K, 233 K, and 235 K, respectively. The simulations shown in the first and second rows are performed with $I_0 = I_{0,H_2}$. The ~~total~~ ice mass (first row (1)) remains largely unaffected by variations in N_0, except the factor 100 downscaling simulation, which shows a significantly reduced ice mass. A notable increase in ice mass is observed with increasing temperature, attributable to ~~the larger absolute amount of water vapor~~ a higher water vapor mass concentration in the atmosphere. This additional water vapor can be deposited onto the ice crystals, thereby increasing their size.

When examining the normalized ice crystal number (second row (2)), we observe a reduction with increasing temperature, primarily in the primary wake. ~~At higher ambient temperatures, the excess water vapor emitted by the engines causes a smaller increase in ice supersaturation in the plume~~ Although the ice crystals grow larger during the first seconds due to the ~~nonlinear relationship between saturation vapor pressure and temperature. Also, this leads to a greater decrease in relative humidity~~ higher water vapor concentration at higher temperatures, they experience, in absolute terms, a stronger increase of the saturation pressure within the descending vortices, ~~resulting in an increased sublimation . Hence, ice crystals are more prone to sublimation in the primary wake at higher ambient temperatures~~ leading to increased sublimation (Unterstrasser, 2016; Bier and Burkhardt, 2022). This phenomenon is most pronounced in the N_0-upscaling cases.

The sensitivity of the survival fraction to the ambient relative humidity and ambient temperature is illustrated in the bottom row (3). In addition to the default cases with $I_0 = I_{0,H_2}$, data points for the kerosene reference case with $I_0 = I_{0,kero}$ are displayed for ~~$T_{amb} = 217\,K$~~ $T_{CA} = 217\,K$ and 225 K (~~see~~ yellow symbols). Simulations with $I_0 = I_{0,H_2}$ indicate that ice crystals, which would typically sublimate under $I_{0,kero}$ conditions, are now sufficiently large to withstand adiabatic heating. This effect is most pronounced in the $RH_{i,amb} = 110\,\%$, N_0-downscaling scenarios (the differences between the yellow and the colored squares are larger than the differences between the yellow and colored circles at ~~$N_0 \leqslant 10^{13}\,m^{-1}$~~ $N_0 \lesssim 10^{13}\,m^{-1}$). Simulations at a lower ambient relative humidity (squared symbols) show a stronger loss of ice crystals, a trend consistent across the variations regarding N_0 and I_0. This is due to the stronger sublimation effects in the primary wake in case of a reduced relative humidity value (Unterstrasser et al., 2014; Unterstrasser, 2016). Notably, in the extreme N_0-downscaling scenario ($N_0 \sim 10^{10}\,m^{-1}$) at 120 % relative humidity, the survival fraction remains largely unaffected by the ambient temperature, with survival fractions equal or close to one at both 217 K ($f_{N,s} = 1.00$) and 235 K ($f_{N,s} = 0.95$). In contrast, for the extreme N_0-upscaling scenario, the impact of ambient temperature is significantly more pronounced, reducing the survival fraction by a factor of 4.5, from $f_{N,s} = 0.09$ at 217 K down to $f_{N,s} = 0.02$ at 235 K. This temperature sensitivity is further amplified in drier atmospheric conditions, where the effect on the survival fraction is more substantial. For the N_0-downscaling scenario, the survival fraction decreases by a factor of 2.24, while in the N_0-upscaling case, the reduction exceeds even one order of magnitude. In the upscaling cases with ambient temperatures at or above 230 K, nearly all ice crystals sublimate, with $f_{N,s} < 0.15$. Initial differences in N_0 spanning four orders of magnitude are reduced to 2.98 (217 K, 120 %) and 2.85 (217 K, 110 %), and further

decrease to 2.37 (235 K, 120 %) and 2.14 (235 K, 110 %), highlighting the importance of both parameters in the context of ice crystal loss during the vortex phase.

The third ambient parameter varied in this study is stratification. Following e.g. Unterstrasser et al. (2014), we use a Brunt-Väisälä frequency of $N_{\mathrm{BV}} = 1.15 \times 10^{-2}\,\mathrm{s}^{-1}$ as the default, and a smaller value, $N_{\mathrm{BV}} = 0.5 \times 10^{-2}\,\mathrm{s}^{-1}$, which characterizes an atmosphere with weaker atmospheric stability. The simulation domain needs to be larger in the latter case as the downward movement and oscillation of the vortex system are stronger. Therefore, to reduce the number of simulations and associated computational costs, we varied N_0 only by a factor of 100 (both up and down). This simulation set is performed only for ~~$T_{\mathrm{amb}} = 217\,\mathrm{K}$~~ $T_{\mathrm{CA}} = 217\,\mathrm{K}$.

Figure 5 displays normalized vertical profiles of the final ice crystal number (panel (a)) and number of sublimated ice crystals (panel (b)) for both stratification scenarios (indicated by linestyle). Only simulations with $I_0 = I_{0,\mathrm{H_2}}$ are displayed here. Evidently, in a weakly stratified ambient atmosphere, the wake vortices generally descend further down. Consequently, sublimation extends to lower altitudes (especially in the default and N_0-downscaling cases, displayed by the black and blue curves). This is mainly observed in the simulations with default or lower N_0 value as the difference in the final contrail height is about 200 m, compared to about 50 m in the N_0-upscaling scenario. This reduced difference in the N_0-upscaling case is because most ice crystals are lost at higher altitudes, independently of stratification. As anticipated, the survival fraction is reduced for contrails evolving in a weakly stratified atmosphere. Decreasing the ambient relative humidity exacerbates crystal loss further. Also, lower survival fractions are observed in scenarios with $I_0 = I_{0,\mathrm{kero}}$, as previously noted (not shown). The original four orders of magnitude difference in N_0 decreases to 2.69 and 2.46 (default and weakly stratified, 120 %), and 2.46 and 2.31 (110 %) at $I_0 = I_{0,\mathrm{kero}}$, as well as 2.98 and 2.72 (120 %), and 2.85 and 2.66 (110 %) at $I_0 = I_{0,\mathrm{H_2}}$.

3.2.2 Sensitivity to the microphysical initialization

We prescribe the initial ice crystal size distribution (SD) as a lognormal distribution with a specified width parameter r_{SD}, see e.g. Unterstrasser and Sölch (2010). A variation of r_{SD} has been shown to have a non-negligible effect on the contrail's evolution during the vortex phase (Unterstrasser, 2014). Varying the width, we adjust the geometric mean diameter such that the total initial ice mass and ice crystal number are unaffected (Unterstrasser, 2014).

In Fig. 6, we present simulations, where r_{SD} is varied according to Tab. 1. The final contrail height for each N_0 scenario appears relatively unaffected by variations in r_{SD}, as shown in Fig. 6(a). However, a narrower initial SD leads to a higher number of ice crystals present at lower altitudes (dashed curves). This can be explained by the delayed onset of sublimation, which occurs at lower altitudes (see panel (b)). In contrast, a broader initial SD results in a higher proportion of smaller ice crystals at the start, which tend to sublimate at higher altitudes, leading to lower survival fractions. This pattern is observed consistently across all N_0 scenarios. To assess the robustness of these results with respect to ambient temperature, we repeated this set of simulations at ~~$T_{\mathrm{amb}} = 233\,\mathrm{K}$~~ $T_{\mathrm{CA}} = 233\,\mathrm{K}$. The general trends related to r_{SD} remain unchanged by the variation in ambient temperature. However, as expected based on previous findings, we observe lower survival fractions at this temperature.

In aircraft plumes characterized by negligible soot emission, such as those from hydrogen-powered engines, ice nucleation is assumed to predominantly occur on entrained ambient aerosol particles (Bier et al., 2024). The dry radii of these ambient

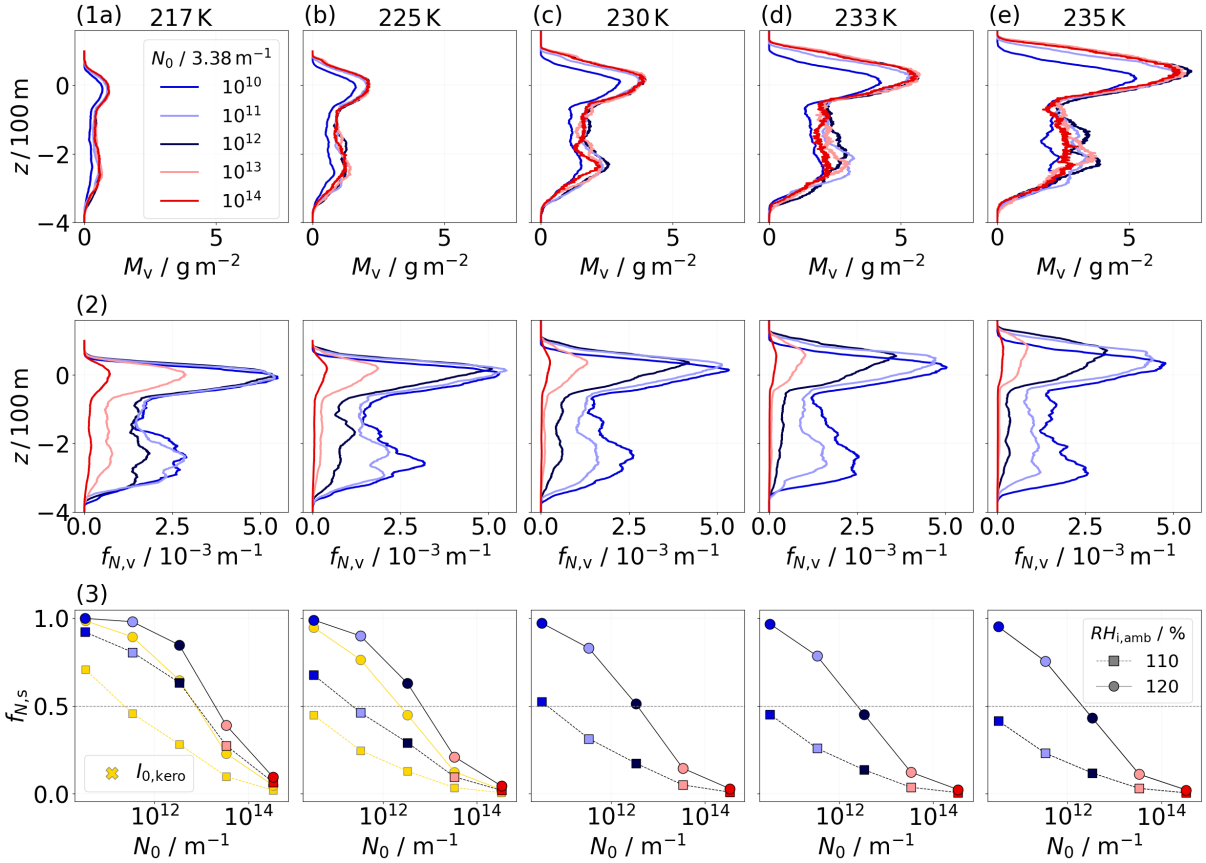

Figure 4. Final vertical profiles of ice mass (first row) and normalized ice crystal number (second row) for different N_0 values (as given in the legend in panel (1a)) after six minutes. Columns depict results for ambient temperatures of 217 K, 225 K, 230 K, 233 K, and 235 K (see titles on top). The ambient relative humidity is 120 %. The third row displays the survival fraction at the two different humidity values as indicated in panel (3e). At ~~$T_{amb} = 217$ K~~ $T_{CA} = 217$ K and 225 K, yellow symbols, which refer to simulations with $I_0 = I_{0,kero}$, are plotted for comparison. A horizontal dashed line at $f_{N,s} = 0.5$ is provided as a visual guide.

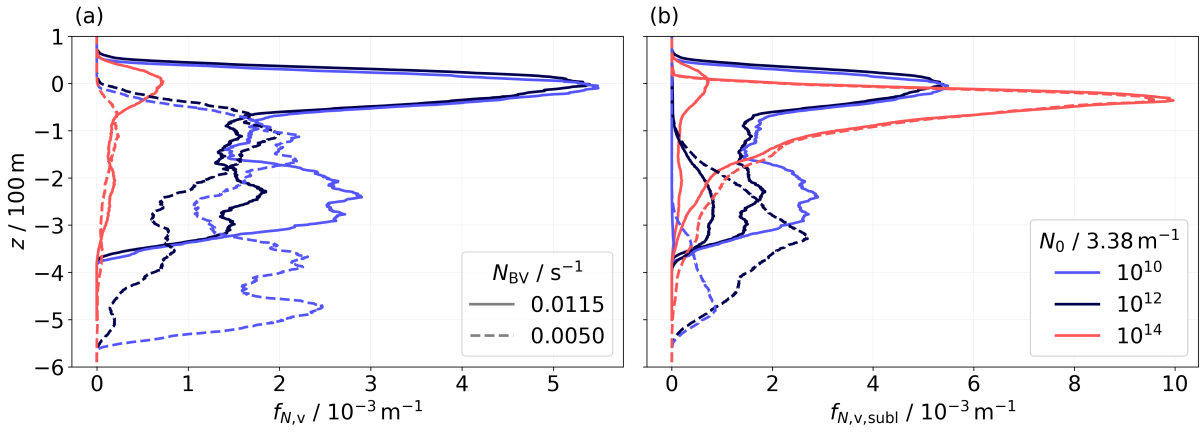

Figure 5. ~~Normalized~~ Final vertical profiles of normalized number of ~~final~~ ice crystals (panel (a)) and normalized number of ~~final~~ sublimated ice crystals ~~in the vertical direction are shown in panels~~ (a) ~~and~~ panel (b)~~, respectively~~). Results for default (solid lines) and weaker (dashed lines) atmospheric stability are depicted. The displayed simulation results correspond to ~~$T_{amb} = 217$ K~~ $T_{CA} = 217$ K, $RH_{i,amb} = 120\,\%$, and $I_0 = I_{0,H_2}$.

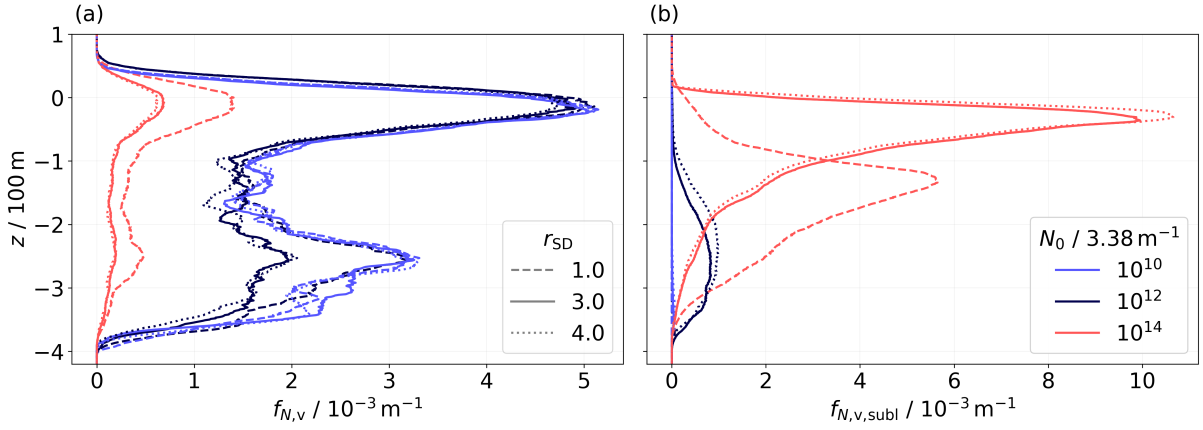

Figure 6. ~~Normalized~~ Final vertical profiles of normalized number of ~~final~~ ice crystals (panel (a)) and normalized number of sublimated ~~final~~ ice crystals ~~in the vertical direction are shown in panels~~ (a) ~~and~~ panel (b)). Solid lines represent the reference cases with $r_{SD} = 3.0$, while initially broader and narrower size distributions are depicted by dotted and dashed lines, respectively. ~~Results~~ The shown simulations were conducted for ~~$T_{amb} = 217$ K~~ $T_{CA} = 217$ K, $RH_{i,amb} = 120\,\%$, and $I_0 = I_{0,H_2}$ ~~are displayed~~.

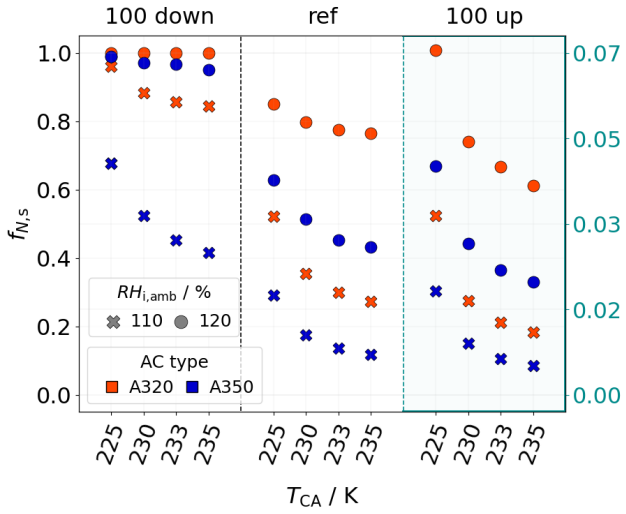

Figure 7. Survival fractions of an A320 (red) and an A350 (blue) aircraft. The three boxes represent the ice crystal number scaling as indicated in the title, where ~~,~~e.g. "100 down" refers to the simulation ~~where~~ with N_0 ~~is~~ equal to $3.38 \times 10^{10}\,\mathrm{m}^{-1}$ (A350) or $0.85 \times 10^{10}\,\mathrm{m}^{-1}$ (A320). In the case of a factor 100 upscaling, the survival fractions are small. Hence, we adapted the axis as indicated by the light blue labels. Simulation results for both values of ambient relative humidity are shown (symbol).

aerosols, therefore, govern the size of the resulting ice crystals. Bier et al. (2024) identified several aerosol modes with sizes spanning from few nanometers to several micrometers. This broad size range is more accurately captured by an initial size distribution with larger values of r_{SD} (e.g. 3.0 and 4.0), thus considered more representative of the physical conditions.

3.2.3 Sensitivity to aircraft type

H_2-contrail simulations for a smaller ~~A320aircraft with~~ A320 aircraft with a wing span of $b_{span} = 34.4\,\mathrm{m}$ are performed for ~~$T_{amb} \geq 225\,\mathrm{K}$~~$T_{CA} \geq 225\,\mathrm{K}$. The grid spacing is adapted as outlined in Tab. 1. We simulate this aircraft type only with a N_0-scaling factor of 100.

Unterstrasser and Görsch (2014) have done baseline simulations for an A320 aircraft in typical kerosene conditions. As revealed in this study, the altitude where sublimation starts is independent of the aircraft type. As ~~the~~ described in Sec. 2.2, both N_0 and I_0 are linearly dependent on the fuel flow rate. Since EI_{iceno} and EI_{H_2O} are assumed to be constant across all aircraft types, the mean mass and radius of the initial ice crystals are consequently independent of the aircraft type, as both are proportional to the ratio I_0/N_0. However, the vortex system of the A320 descends more slowly. Therefore, the sublimation threshold altitude is reached later. The vortices of the A320 dissolve before such low altitudes can be reached, where strong sublimation occurs. This decreases sublimation effects in the primary wake, allowing more ice crystals to survive the vortex phase for smaller aircraft like the A320 than larger ones like the A350. This trend holds across all N_0-scaling scenarios.

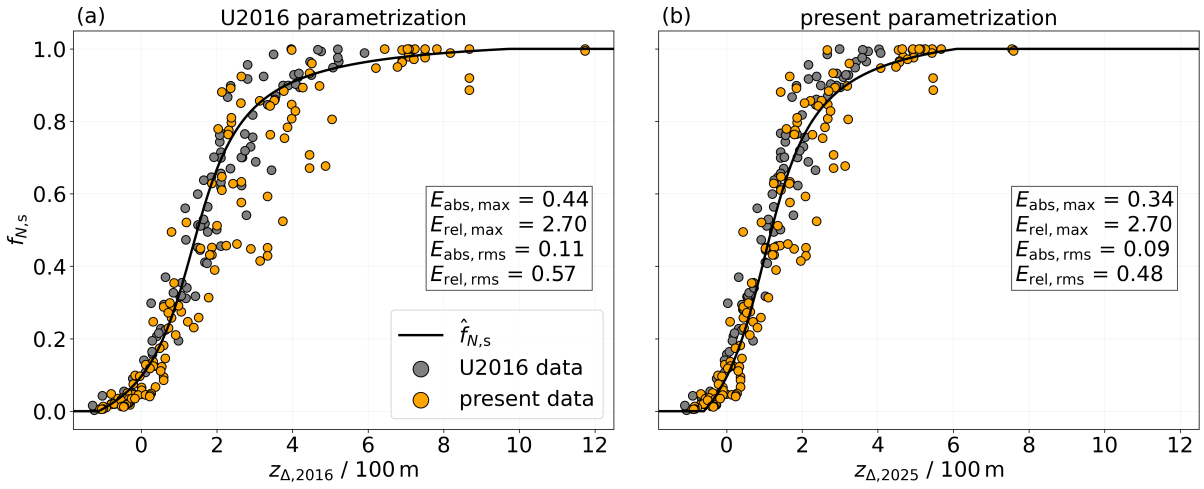

Figure 8. Simulated survival fraction as a function of the parameter z_Δ. The original (a) and updated (b) parametrizations are denoted by the solid black line. Grey points represent the simulated survival fractions from the 2016 study, while orange points correspond to those from the present study. Since the fit coefficients are adapted in the new formulation, the z_Δ parameter differs in both versions, denoted by $z_{\Delta,2016}$ and $z_{\Delta,2025}$.

Although the final A350 contrail still contains more ice crystals than the A320 contrail, the relative ice crystal loss is greater for the A350, reducing the initial large differences in ice crystal numbers.

~~As described in Sec. 2.2, both N_0 and I_0 are linearly dependent on the fuel flow rate. Since EI_{iceno} and EI_{H_2O} are assumed to be constant across all aircraft types, the mean mass and radius of the initial ice crystals are consequently independent of the aircraft type, as both are proportional to the ratio I_0/N_0. Despite growing larger in the first few seconds in the A350 case due to the larger water vapor emission, more ice crystals are lost within the descending vortices. The stronger vertical displacement of the primary wake and the associated sublimation there outweigh the initial higher ice crystal growth rate, leading to a more significant overall ice crystal loss.~~

Figure 7 shows how the survival fractions depend on the aircraft type. Each box, delineated by the dashed vertical lines, corresponds to a different N_0-scaling scenario. Note that in the factor 100 upscaling scenario, where the survival fractions are less than 0.1, the y-axis is adjusted accordingly. For each scenario, simulations at ~~$T_{amb} = 225\,K$~~$T_{CA} = 225\,K$, 230 K, 233 K, and 235 K are performed, as indicated on the x-axis. As discussed in Sec. 3.2.1, high ambient temperatures and low relative humidity increase ice crystal loss. Overall, the A320 exhibits higher survival fractions, with the most pronounced differences at low N_0 values and low ambient humidity (e.g. $f_{N,s} = 0.84$ for the A320 and $f_{N,s} = 0.42$ for the A350 at ~~$T_{amb} = 235\,K$~~$T_{CA} = 235\,K$). In scenarios with a strong N_0 upscaling, nearly all ice crystals sublimate regardless of aircraft type ($f_{N,s} \leq 0.07$).

3.3 Parametrization of ice crystal loss

Unterstrasser (2016, from now on U2016) presents an ice crystal loss parametrization that approximates the survival fraction of ice crystals after the vortex phase $f_{N,\mathrm{s}}$ and takes into account the impact of ambient relative humidity, temperature at cruise altitude, thermal stratification, apparent ice crystal emission index, and aircraft parameters. Relevant aircraft parameters are the water vapor emission I_0, the wing span b_{span}, and the wake vortices' initial circulation Γ_0. A typical application of the parametrization is the implementation in larger scale contrail models where the contrail initialization refers to some state after vortex break-up, and effects of the wake dynamics cannot be explicitly resolved. The development of the parametrization was based on a database of > 80 EULAG-LCM simulations, which are sensitivity studies with variations of the parameters above. Notably, the focus at that time was on contrails from kerosene combustion. The new set of H_2-contrail simulations investigates the sensitivity to N_0 more systematically and over a broader range. Moreover, contrails at temperatures above 225 K have not been considered previously, and the validity of the parametrization beyond this temperature threshold is not guaranteed.

The following paragraphs will briefly repeat the parametrization formulation, describe appropriate adaptations, and analyze its applicability and performance for the new H_2-contrail data set.

The ice crystal loss during the vortex phase can be assessed by introducing three length scales that describe the processes relevant to downward propagating contrail ice crystals.

- z_{desc} is the final vertical displacement of the wake vortex system, which leads to a maximum adiabatic heating experienced in the primary wake. The quantity depends most strongly on thermal stratification, aircraft mass, and wingspan.
- z_{atm} measures the effect of the ambient supersaturation on the ice crystal mass budget. z_{atm} is the distance an air parcel has to travel down until its saturation pressure equals its vapor pressure (i.e. until its supersaturation is depleted due to adiabatic heating). The quantity depends most strongly on the ambient relative humidity.
- z_{emit} measures the effect of the water vapor emission on the ice crystal mass budget. Analogously to z_{atm}, z_{emit} corresponds to an adiabatic heating such that an initially saturated parcel remains at saturation when the emitted water vapor is added to the parcel. The quantity depends on the ambient temperature and the amount of emitted water vapor, which in turn depends on the fuel consumption, the emission index of water vapor, and the contrail cross-section.

The exact definitions of these length scales are given in Sec. 3.1 of U2016. ~~However,~~ We repeat the definition of z_{desc}, which is given by

$$z_{\mathrm{desc}} = \left(\frac{8\Gamma_0}{\pi N_{\mathrm{BV}}} \right)^{1/2} . \tag{6}$$

Regarding z_{atm} and z_{emit}, we implement slightly redefined formulae. In the previous version, the definitions of z_{atm} and z_{emit} are based on the assumption of balancing water vapor concentrations. In the updated parametrization, we redefine the two length scales by requiring the conservation of water vapor mass mixing ratios, which are the quantities that are actually conserved

under adiabatic changes. Hence, we introduce the adiabatic index $\kappa = 3.5$, and the modified equations read as

$$(1 + s_\mathrm{i})\,\frac{e_\mathrm{s}(T_\mathrm{CA})}{{T_\mathrm{CA}}^{\kappa}} = \frac{e_\mathrm{s}(T_\mathrm{CA} + \Gamma_\mathrm{d}\, z_\mathrm{atm})}{(T_\mathrm{CA} + \Gamma_\mathrm{d}\, z_\mathrm{atm})^{\kappa}} \tag{7}$$

and

$$\frac{e_\mathrm{s}(T_\mathrm{CA})}{R_\mathrm{WV}\,{T_\mathrm{CA}}^{\kappa}} + \frac{\rho_\mathrm{emit}}{{T_\mathrm{CA}}^{\kappa-1}} = \frac{e_\mathrm{s}(T_\mathrm{CA} + \Gamma_\mathrm{d}\, z_\mathrm{emit})}{R_\mathrm{WV}\,(T_\mathrm{CA} + \Gamma_\mathrm{d}\, z_\mathrm{emit})^{\kappa}}. \tag{8}$$

Γ_d is the dry adiabatic lapse rate, with a value of 9.8 ~~K~~K km^{-1}. The water vapor saturation pressure is represented by e_s, and $s_i = RH_\mathrm{i} - 1$ denotes the supersaturation. According to U2016, we then define a linear combination of these length scales

$$z_\Delta = \tilde{\alpha}_\mathrm{atm}\, z_\mathrm{atm} + \tilde{\alpha}_\mathrm{emit}\, z_\mathrm{emit} - \tilde{\alpha}_\mathrm{desc}\, \hat{z}_\mathrm{desc} \tag{9}$$

with positive weights $\tilde{\alpha}_\mathrm{X}$.

z_Δ is large if the buffer effect of the ambient supersaturation and the emitted water vapor outweighs the adiabatic heating due to the wake vortex descent. This means, the water vapor surplus is sufficient to keep the heated air parcel supersaturated. [*Side remark: Note that in the simulations, the air parcel does not remain supersaturated, but RH_i quickly relaxes to 100 %. Figure 3b reveals that the water vapor surplus deposits on the ice crystals within a few seconds (for large N_0) or within at most 30 s (for low N_0). The local maximum attained within the first half a minute clearly relates to the water vapor surplus as estimated by the two length scales z_{atm} and z_{emit}. Note that the increase in ice mass after two minutes is due to detrained ice crystals outside of the vortex system, which grow in the supersaturated ambient air. Figure 2a in Unterstrasser and Sölch (2010) displays the evolution of the total ice mass in the descending wake vortex system. This nicely reveals the dependence of the peak value on the water vapor surplus and the subsequent monotonic decrease of the ice mass. Hence, the buffer effect is achieved by increasing the total mass and the mass concentrations of the ice crystals in the vortex system. The larger those quantities are after the initial growth period, the more and the longer the ice crystals can shrink until complete sublimation.*]

A small z_Δ (including also negative values) means that the wake vortex descent prevails for so long that a substantial fraction or even all the entrained ice crystals are likely lost.

Following U2016, both $\tilde{\alpha}_\mathrm{atm}$ and $\tilde{\alpha}_\mathrm{emit}$ are modified to include the effect of a variation of N_0, while $\tilde{\alpha}_\mathrm{desc}$ can be left unchanged (i.e. $\alpha_\mathrm{desc} = \tilde{\alpha}_\mathrm{desc}$):

$$z_\Delta = \Psi^{\gamma}(\alpha_\mathrm{atm}\, z_\mathrm{atm} + \alpha_\mathrm{emit}\, z_\mathrm{emit}) - \alpha_\mathrm{desc}\, \hat{z}_\mathrm{desc}. \tag{10}$$

In U2016, Ψ was given by $\frac{1}{\mathrm{EI}^*_\mathrm{iceno}}$ with $\mathrm{EI}^*_\mathrm{iceno} = \frac{\mathrm{EI}_\mathrm{iceno}}{\mathrm{EI}_\mathrm{iceno,ref}}$ and a positive constant γ. In the new formulation, Ψ is defined as

$$\Psi = 1/n_0^*, \tag{11}$$

where n_0 is an (intermediate) ice crystal number concentration and the starred quantity is the value normalized by a reference value $n_{0,\mathrm{ref}}$. In both approaches, increasing $\mathrm{EI}_\mathrm{iceno}$ (in the original formulation) or n_0 (in the new formulation) gives smaller weights $\tilde{\alpha}_\mathrm{atm}$ and $\tilde{\alpha}_\mathrm{emit}$. This reduces the buffer effect and, consequently, z_Δ. This reflects the fact that ice crystal loss becomes

more substantial when the water vapor surplus is distributed over more ice crystals with smaller masses on average. With smaller mean ice crystal sizes, a specific fraction of lost ice mass translates into a larger relative fraction of lost ice crystals.

The definition of n_0 is deferred to the Appendix (Eq. (A1)) and the motivation for the switch from $\mathrm{EI}^*_{\mathrm{iceno}}$ to n_0^* is explained in Sec. 4.

The three length scales depend only on input parameters and can be evaluated for given meteorological and aircraft properties. Notably, they are independent of N_0, and the sensitivity of z_Δ to N_0 enters the parametrization solely by an adaptation of the weights $\tilde{\alpha}_{\mathrm{atm}}$ and $\tilde{\alpha}_{\mathrm{emit}}$.

Plotting the simulated $f_{N,\mathrm{s}}$ values as functions of z_Δ with suitably chosen weights, the data points can be reasonably well approximated by an arc tangent function. Hence, the parametrized survival fraction $\hat{f}_{N,\mathrm{s}}$ can then be defined as

$$\hat{f}_{N,\mathrm{s}} = \hat{a}(z_\Delta), \tag{12}$$

with

$$\hat{a}(x) = \beta_0 + \frac{\beta_1}{\pi} \arctan\left(\alpha_0 + (x/100\,\mathrm{m})\right). \tag{13}$$

In the following, we outline our procedure for determining the new set of fit coefficients. Simulations with $r_{\mathrm{SD}} = 1.0$ and $r_{\mathrm{SD}} = 4.0$, accounting for approximately 25 % of the total dataset, were excluded from the fitting process, as they represent extreme cases of the size distribution width. However, these simulations are still shown in Fig. 8. We selected a representative subset of simulations using the default value of $r_{\mathrm{SD}} = 3.0$. Additionally, some data points from simulations with weaker stability were identified as outliers and excluded. Consequently, 69 % of the new simulations and the entire data set from U2016 were used to derive the fit coefficients. A weighting was applied in the fitting procedure, with all data points at $RH_{\mathrm{i,amb}} = 110\,\%$ and $\mathrm{EI}^*_{\mathrm{iceno}} > 1$ being assigned higher weights (1.1 and 2.0, respectively). On the one hand, these weights were introduced to reduce the absolute errors of the $RH_{\mathrm{i,amb}} = 110\,\%$ cases. This is favorable as the survival fractions are systematically smaller than for the $RH_{\mathrm{i,amb}} = 120\,\%$ cases. Hence, similar absolute errors over both sets of simulations would imply larger relative errors for $RH_{\mathrm{i,amb}} = 110\,\%$ cases. Furthermore, the occurrence frequency of ice supersaturation is exponentially distributed with decreasing encounter probabilities for increasing $RH_{\mathrm{i,amb}}$ values (Petzold et al., 2017). Increasing the weights is a pragmatic solution to put more emphasis on the low-$RH_{\mathrm{i,amb}}$ cases.

We propose the following values for the fitting coefficients:

$$\beta_0 = 0.42, \tag{14a}$$

$$\beta_1 = 1.31, \tag{14b}$$

$$\alpha_0 = -1.00, \tag{14c}$$

$$\alpha_{\text{atm}} = 1.27, \tag{14d}$$

$$\alpha_{\text{emit}} = 0.42, \tag{14e}$$

$$\alpha_{\text{desc}} = 0.49, \tag{14f}$$

$$\gamma = 0.16. \tag{14g}$$

Figure 8 presents a comparison between both versions, where the simulation data used to derive the original parametrization formulation are displayed in grey, and the present (additional) data points are shown in orange. Panel (a) depicts the 2016 parametrization curve. The new parametrization (panel (b)) reduces both the absolute maximum and root mean square error (see values inserted in the figure). The absolute root mean square is reduced by 2 %, whereas the relative root mean square error of the U2016 data is decreased by 9 %. Relative to the U2016 database, the new H_2 simulations sample particularly the space for large and very small $f_{N,\text{s}}$ values more densely. The supplement contains further plots that help to rate the changes implied by the new version.

In Fig. 9, we show the updated parametrization for various meteorological and aircraft scenarios. As indicated by its title, each panel highlights specific sensitivity analyses. The dependencies of the survival rate on the input parameters have been thoroughly explained in the preceding sections. The following will discuss the new insights gained from the updated parametrization. It can be observed that simulations performed at temperatures above 225 K are well represented by the parametrization. This holds for both the N_0-upscaling and -downscaling scenarios. While a critical temperature exists above which contrail formation is not possible, this temperature threshold has no direct relevance for the microphysical processes during the vortex phase. Hence, it is not surprising that the validity of the parametrization extends beyond 225 K.

The parametrization does not account for variations in r_{SD}, meaning that data points from simulations with different r_{SD} values but the same z_Δ value are treated identically. Notably, for N_0-upscaling cases, simulations with $r_{\text{SD}} = 1.0$ tend to show survival fractions that are somewhat overestimated. For the time being, this is an irreducible uncertainty partly due to idealizations in our initialization.

Regarding aircraft type, the parametrization effectively represents both A350 (bluish) and A320 (reddish) cases across upscaling and downscaling scenarios, as shown in panels (f) and (g). Additionally, the parametrization is consistent with other simulation results from studies such as Lewellen et al. (2014) and Picot et al. (2015), as highlighted in panel (h). Our updated H_2 parametrization not only aligns well with these results, but also particularly captures the ice crystal emission index variation study from Lewellen (2014), further demonstrating the validity of the new parametrization.

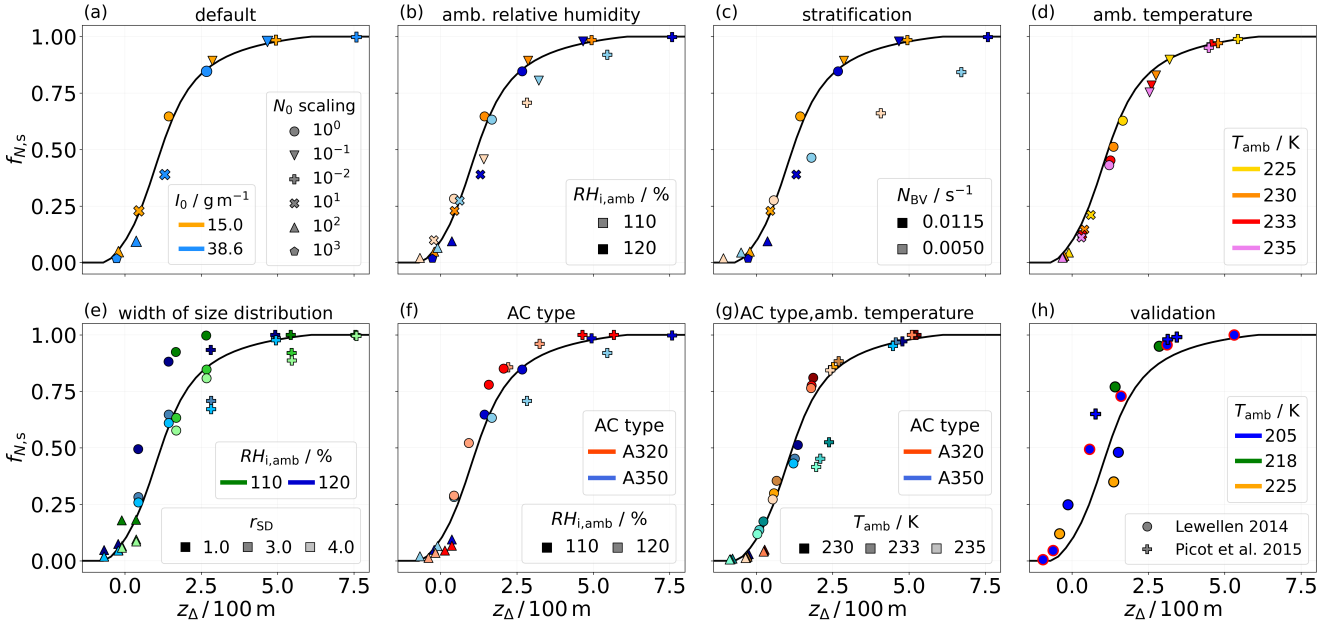

Figure 9. Simulated survival fractions as functions of the parameter z_Δ ($= z_{\Delta,2025}$), focusing exclusively on new H_2 simulations. The symbol legend in panel (a) applies to the panels (a)-(g), with symbols indicating N_0-scaling information. In panels (a)-(c), blue symbols denote hydrogen water vapor emissions, while orange symbols represent kerosene cases. Each panel highlights a different meteorological or aircraft scenario, as the titles indicate. Panel (h) displays survival fractions from other studies for comparison and validation. There, symbols with a red outline correspond to a study investigating the effects of varying the ice crystal emission index (Lewellen et al., 2014).

3.4 Impact of vortex phase processes on contrail-cirrus evolution

This section presents results of contrail-cirrus simulations and demonstrates the relevance of the ice crystal number in young contrails for the subsequent transition into contrail-cirrus.

We employ the EULAG-LCM model in a setup largely based on that used in Unterstrasser et al. (2017a) and Unterstrasser et al. (2017b). We use a domain with two dimensions, x (horizontal) and z (vertical), that is perpendicular to the direction of flight. We embed the data of the vortex phase simulation (averaged along the flight direction) in a significantly larger simulation domain spanning 40 km in x- and 2.5 km in z-direction, with grid resolutions of $\mathrm{d}x = \mathrm{d}z = 10\,\mathrm{m}$. The simulated time is 8 h. ~~While sedimentation was switched off in the vortex phase simulation, it is switched on here as it is a crucial process in the contrail-cirrus transition.~~ The sedimentation velocities are determined using the Reynolds number and the maximum particle dimensions, as described in the Appendix of Sölch and Kärcher (2010). We prescribe a stepwise vertical profile of relative humidity, assuming an ambient ice supersaturated layer of 120 % between 1 and 2 km (see further details in, e.g., Unterstrasser et al. (2017a)). We also impose a synoptic-scale updraught (with an updraught velocity $w = 1\,\mathrm{cm\,s^{-1}}$) over roughly six hours, leading to a final adiabatic cooling of 2 K. We choose an A350 aircraft with ~~$T_{amb} = 225\,K$~~ $T_{CA} = 225\,\mathrm{K}$, $N_{BV} = 1.15\times10^{-2}\,\mathrm{s^{-1}}$,

$I_0 = I_{0,\mathrm{H_2}}$, and $r_{\mathrm{SD}} = 3.0$. In the first simulation series, the contrail-cirrus initialization is directly based on the results from the according vortex phase simulation. The initialized contrail consists of $N = f_{N,\mathrm{s}} \times N_0$ ice crystals. In the second simulation series, we deliberately disregard vortex phase loss processes and initialize a contrail with N_0 ice crystals. This is accomplished by using the contrail data from the first simulation series and uniformly scaling up the ice crystal number concentrations by a factor of $(f_{N,\mathrm{s}})^{-1}$.

An important quantity for analyzing contrail evolution is the total extinction, which serves as a metric for the radiative effect of an individual contrail (Unterstrasser, 2020). It is defined as the horizontal integral of the extinction, $1 - \exp(-\tau)$, where τ represents the optical thickness along the vertical direction. ~~Mathematically, it~~ Then, total extinction is expressed as:

$$\begin{aligned} E(t) &= \int (1 - \exp(-\tau(x,t)))\,\mathrm{d}x \approx \int \tau(x,t)\,\mathrm{d}x \\ &= \iint \chi(x,z,t)\,\mathrm{d}z\,\mathrm{d}x, \end{aligned} \tag{15}$$

where $\chi(x,z,t)$ is the extinction coefficient. It is proportional to the projected area of the ice crystals per unit volume. We assume an extinction efficiency $Q_{\mathrm{ext}} = 2$, as described in Schumann et al. (2011). Figure 10 illustrates the temporal evolution of the total ice crystal number (panel (a)) and the total extinction (panel (b)). In both panels, the color represents the N_0 scaling, with red indicating upscaling scenarios and blue denoting downscaling scenarios. The line style differentiates between the two setups.

Three key observations emerge: Firstly, E is significantly higher in the N_0-upscaled scenarios. This outcome is expected, as total extinction is proportional to the effective surface area of the ice crystals; a larger number of ice crystals, as shown in panel (a), leads to a greater extinction. Secondly, the contrail(-cirrus) dissipates more quickly when N_0 is smaller. In the scenario where N_0 is reduced by a factor of 100 (dark blue), the contrail disappears after only few hours, indicating a significantly shorter lifetime. Thirdly, we observe an increase in E in the scenarios where the vortex phase losses are disregarded. In these cases, the contrail is initialized with more ice crystals compared to the first simulation series (see panel (a)).

A qualitative comparison of the two setups can be made by examining the lifetime-integrated total extinction values, $\hat{E} = \int E(t)\,\mathrm{d}t$, that are displayed in Fig. 11(a). Ignoring vortex phase losses leads, at maximum, to a difference in lifetime-integrated total extinction of 46 %. This indicates that the radiative impact of an individual contrail can be significantly overestimated if vortex phase processes, such as contrail expansion and ice crystal sublimation in the primary wake, are not considered. The ~~non-linear~~ nonlinear increase in the $\hat{E}$ difference between both setups in the N_0-upscaled simulations may be attributed to saturation effects. As the number of ice crystals increases, competition for available water vapor in the spreading contrail-cirrus becomes more important. Consequently, the peak ice mass does not continue to grow indefinitely with increasing N_0 values but is expected to reach a limit eventually. This explains why the simulation with a 100-fold increase in N_0 shows a smaller increase in lifetime-integrated total extinction when disregarding the vortex phase losses compared to the simulation with a 10-fold increase in N_0. We repeated this kind of simulation series, i.e. disregarding the crystal losses from the vortex phase, for the $I_{0,\mathrm{kero}}$ scenario. Interestingly, we observe only a small impact on the lifetime-integrated total extinction when the vortex phase losses are ignored (see Fig. 11(b)). This suggests that the initial water vapor emission, compared to the ice crystal number, has only a minor impact on the radiative effect of a single contrail-cirrus.

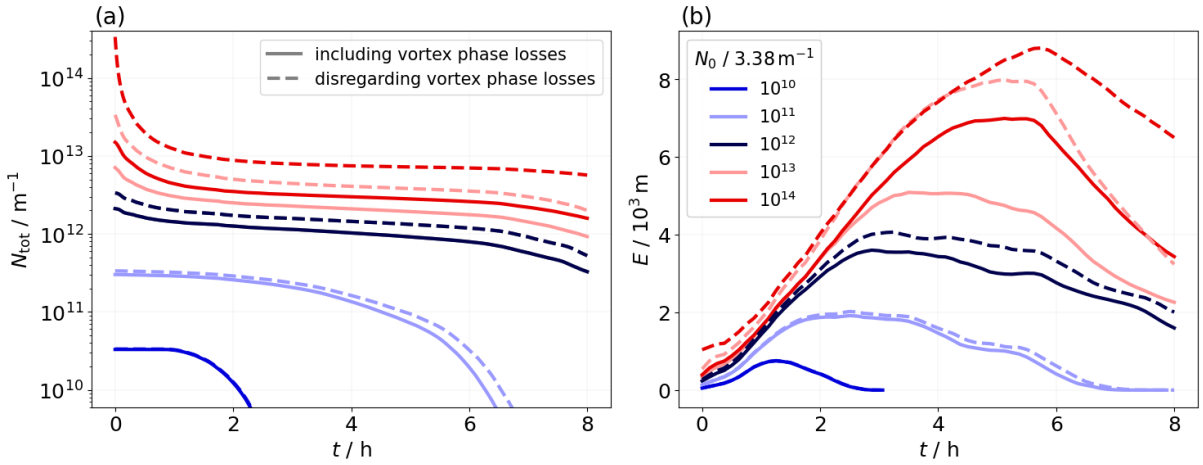

Figure 10. Time evolution of the total number of ice crystals (a) and total extinction (b) for the N_0 ~~up-~~ up- and downscaling cases. In the first simulation series, the contrails are initialized by using the final state from the respective vortex phase simulations; in the second simulation series, the ice crystal numbers are upscaled by the respective survival fractions.

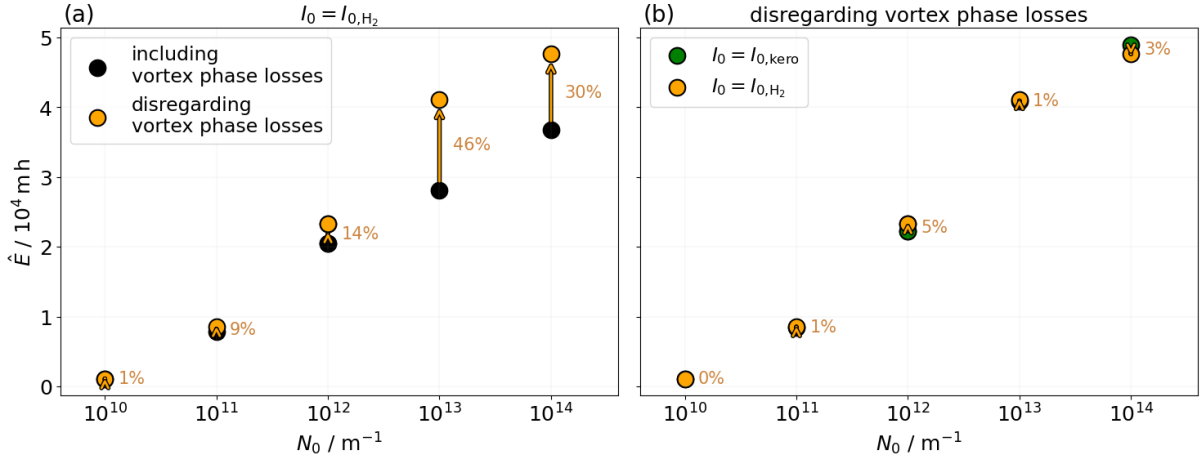

Figure 11. Lifetime-integrated total extinction $\hat{E}$ for all five N_0-scaling scenarios. Panel (a) highlights the increase of this quantity in the second simulation series (shown by the orange points). Panel (b) displays $\hat{E}$ for both I_0 options. The orange points are the same in both panels.

This is just one example of a contrail-cirrus simulation set. A comprehensive analysis, examining various meteorological parameters, will follow.

4 Discussion

This study highlights the importance of ice crystal loss during the vortex phase depending on the propulsion system. While previous research has examined the effect of initial ice crystal numbers on crystal loss — such as Lewellen (2014), who varied the ice crystal emission index across six orders of magnitude, and Unterstrasser (2014), who explored a variation over two orders of magnitude — this work takes a systematic approach tailored explicitly to H_2 contrails. It uniquely combines variations in the initial number of ice crystals with adjustments to the ~~amount of~~ emitted water vapor mass. The N_0-upscaling scenarios may not only represent a potential H_2 fuel cell setup but also account for the formation of contrail ice crystals on ultrafine volatile particles (UFPs). UFPs, typically nm-sized particles, can contribute to ice crystal formation if the plume supersaturation is high enough to overcome the Kelvin barrier for activation (Kärcher et al., 2015). This requires the reduction of the soot particle number at least 10-fold, preventing them from acting as the primary condensation nuclei for water vapor, and an ambient temperature significantly below the formation threshold (Kärcher, 2018).

In addition to nitrogen species emissions from H_2 engines, oil vapor emissions due to engine lubrication systems are possible (Ungeheuer et al., 2022; Bier et al., 2024). This can lead to the nucleation into ultrafine oil droplets, as observed in measurements (Ungeheuer et al., 2021). Experiments by Ponsonby et al. (2024) explored the potential of lubrication oil droplets to act as contrail ice-forming particles, revealing that these droplets are less effective as condensation nuclei than soot particles within the temperature range of 225–245 K. Nevertheless, the study showed that lubrication oil droplets can competitively deplete plume supersaturation under soot-poor conditions, as their critical supersaturation is readily achievable. In H_2 plumes, these ultrafine oil droplets might contribute to ice crystal formation alongside background aerosols. Further research on the properties of oil droplets, such as their size distribution and emission indices, is necessary to fully understand their potential role in contrail ice crystal formation processes. Yu et al. (2024) highlight that UFPs might significantly contribute to the total number of contrail ice particles if the sizes of the soot particles are reduced. Hence, understanding the role of UFPs in the contrail formation process requires the consideration of both soot emissions and particle sizes. The UFP number could potentially exceed that of emitted soot particles per flight distance, leading to a larger number of nucleated ice crystals in H_2 plumes compared to conventional kerosene plumes (Kärcher et al., 2015; Bier et al., 2024). This justifies our approach of increasing the initial number of ice crystals to capture possible scenarios of additional ice-forming particle sources.

Furthermore, this study addresses a previously unexplored area by analyzing contrail evolution during the vortex phase at temperatures $> 225\,\mathrm{K}$. At higher ambient temperatures, the number of nucleated ice crystals decreases, increasing the number of ice crystals that survive the vortex phase (Bier and Burkhardt, 2022). Since our study design is independent of the specific formation processes, it hypothetically determines the survival fractions for a given fixed N_0.

We revised the original formulation of the vortex loss parametrization by incorporating the conservation of mass mixing ratios, adding a layer of complexity to the equations but ensuring that the physical assumptions are accurately represented. With appropriately chosen parameters, the arc tangent curve fits the data points well, both from the U2016 and present studies. Additionally, the new formulation of the fitting function is designed to account for scenarios where N_0 is significantly upscaled. Although the parametrization is based on the N_0-scaling study spanning four orders of magnitude, it remains applicable even

for more extreme values of N_0. The parametrization also yields plausible results in terms of high ambient temperatures. The updated parametrization does not fully capture specific data points, particularly in cases with decreased stratification and downscaled N_0 values. As the length scale z_{desc} is the quantity that accounts for the variation of atmospheric stability, an adjustment to the formulation of z_{desc}, as initially proposed by Unterstrasser (2014), may be necessary to improve accuracy.

Next, we motivate our new choice for the adaptation factor Ψ in the updated ice crystal loss parametrization. The original version in U2016 was based on simulations that all had the same $\text{EI}_{\text{H}_2\text{O}}$ value, and the emission index EI_{iceno} was a good estimator of the representative ice crystal size in the contrail. A straightforward generalization would be to replace EI_{iceno} by the ratio $\text{EI}_{\text{H}_2\text{O}}/\text{EI}_{\text{iceno}}$ in the definition of Ψ. However, this quantity is only a proxy of the ice crystal mean mass ($:= I_0/N_0 = \text{EI}_{\text{H}_2\text{O}}/\text{EI}_{\text{iceno}}$) when all emitted water vapor deposits on the ice crystals, yet it neglects the contribution from the environment. Keeping in mind that the buffering effect of the two water vapor sources (from emission and from environment) is already captured by z_Δ, we now define Ψ as a proxy for the typical ice crystal number concentration in the primary wake. The exact definition can be found in section A1.

One main goal of our study is to understand and systematically analyze the impact of the initial ice crystal number and of an assumed water vapor emission on the early contrail properties. We neglect any possible changes in aircraft geometry, mass, overall propulsion efficiency, etc., between current kerosene-driven aircraft and future H_2 aircraft. Clearly, such adaptations would affect the strength of the wake vortices and the fuel consumption (in addition to the factor 2.79^{-1} mentioned above). Moreover, H_2 fuel cells produce electric power that drives propellers. Design concepts with different numbers and positions of propellers and exhaust outlets exist in the literature (e.g. Marciello et al., 2023; Tiwari et al., 2024). Understanding the formation and the early evolution of contrails behind a propeller-driven aircraft deserves separate modelling studies. For the time being, we prefer to limit our study to variations of N_0 and I_0 without any other aircraft adaptation in order to avoid complicating and overloading the interpretation of our results.

Once H_2 aircraft designs are less hypothetical, one could incorporate such adaptations (like a systematically higher aircraft mass due to larger tank systems or particular aspects of H_2 fuel cell aircraft) in subsequent modelling studies.

The updated parametrization is now prepared for integration into large-scale global models, where the U2016 parametrization is already implemented (Bier and Burkhardt, 2022). Bier and Burkhardt (2022) underscore the significance of the initial number of ice crystals, highlighting the critical role of our study, which focuses on the vortex phase and ice crystal loss, in assessing the climate impact of H_2 contrails.

5 Conclusions

In this study, we simulated the evolution of contrails up to an age of approximately six minutes using the EULAG-LCM model, a fluid dynamics solver coupled with a particle-based microphysical model. The focus is on contrails produced by hydrogen-powered aircraft, including both hydrogen direct combustion and hydrogen fuel cell systems. The simulations assume that ice crystal formation and vortex roll-up are complete at initialization. We varied the initial number of ice crystals over a wide range spanning four orders of magnitude, from $3.38 \times 10^{10}\,\text{m}^{-1}(0.85 \times 10^{10}\,\text{m}^{-1})$ to $3.38 \times 10^{14}\,\text{m}^{-1}(0.85 \times 10^{14}\,\text{m}^{-1})$ for

an A350/B777-like (A320/B737-like) aircraft. Additionally, we scaled the emitted water vapor by a factor of 2.57 compared to the reference kerosene case. A parameter study was conducted, varying meteorological, microphysical, and aircraft parameters, focusing on the survival fraction / final number of ice crystals, a critical factor influencing subsequent contrail evolution.

Our simulations indicate that ice crystals tend to be larger in contrails from hydrogen-powered aircraft, leading to a higher likelihood of surviving the vortex phase. This effect is also observed in contrails initialized with a very small number of ice crystals, where the limited competition for available water vapor during depositional growth promotes the formation of larger ice crystals. As anticipated in previous studies, we find initial differences in ice crystal number getting reduced after the vortex phase. The higher the initial ice crystal number, the stronger this reduction is. This finding is independent of any meteorological condition. Sublimation driven by adiabatic heating in the descending vortex pair becomes more significant in drier atmospheric conditions, a trend consistent across all N_0 variations. Furthermore, a higher ambient temperature enhances ice crystal sublimation, though the surviving crystals tend to be larger. We find that the temperature sensitivity is particularly pronounced in the N_0-upscaling scenarios. A reduced thermal stratification leads to a more significant loss of ice crystals, with this effect being more pronounced at higher initial ice crystal numbers and in drier atmospheric conditions. A shift towards a narrower initial size distribution generally produces larger ice crystal sizes, thereby reducing the extent to which initial differences are balanced, as we have consistently observed in the H_2 simulations. The weaker vortex descent associated with smaller aircraft results in a reduced sublimation of ice crystals in the primary wake, leading to higher survival fractions in the case of A320 aircraft. This trend is consistent across all N_0 values and ambient temperature scenarios.

We have refined the existing parametrization of ice crystal loss, presented by Unterstrasser (2016), by incorporating a new set of H_2-contrail simulations. Given that the new simulations tend to cluster at the extremes of the parametrization function, we adjusted the fitting procedure to better capture these behaviors. The updated set of fitting coefficients is provided. A comparison with simulation results from other studies demonstrates a good agreement with our updated parametrization.

It is not yet possible to make a definitive assessment of whether flying with hydrogen is advantageous from a contrail perspective. Further research is needed to assess contrail formation processes for hydrogen propulsion, with measurement results (Airbus, 2023) providing essential insights. As shown in Figs. 10 and 11, the initial number of ice crystals has a significant impact on the subsequent characteristics of the contrail. This study aimed to conduct a broad analysis of N_0 during the first six minutes of contrail evolution. Determining more robustly the number of ice crystals formed in the H_2 case remains an active area of research.

The analysis of the complete set of contrail-cirrus simulations (extending the study that is demonstrated in Sec. 3.4), which are based on the H_2-contrail vortex phase simulations presented here, is in progress.

Data availability. The presented data are available from the corresponding author upon request (annemarie.lottermoser@dlr.de)

Appendix A: Details about the ice crystal loss parametrization

A1 Definition of the ice crystal concentration n_0 in the new parametrization

As described in Sec. 3.3, the adaptation factor Ψ accounting for the mean ice crystal size (in the original formulation given by $1/\mathrm{EI}^*_{\mathrm{iceno}}$) is now defined differently. In the new formulation, Ψ is expressed as $\Psi = 1/n_0^*$, where n_0 represents an (intermediate) ice crystal number concentration:

$$n_0 = N_0/A_\mathrm{p}, \tag{A1}$$

where N_0 is the initial ice crystal number (per meter of flight path) and A_p is the intermediate plume cross-sectional area. Hence, n_0 represents an average concentration in the primary wake. We recall $N_0 = m_\mathrm{C} \times \mathrm{EI}_{\mathrm{iceno}}$ (see Eq. (1)) and the empirical relationships (for conventional aircraft designs of different sizes as studied in Unterstrasser and Görsch (2014) and derived in U2016): $m_\mathrm{C} \sim {b_\mathrm{span}}^2$ (Eq. (A9) in U2016) and $A_\mathrm{p} \sim {b_\mathrm{span}}^2$ (Eqs. (A6) and (A7) in U2016), where b_span is the wing span of the aircraft. Hence, n_0 is roughly independent of aircraft type, but depends linearly on $\mathrm{EI}_{\mathrm{iceno}}$. Note that the empirical relation for A_p is derived from the simulation results and is not supposed to be adapted. The actual fuel consumption m_C may, however, deviate from the empirical relationship (representing typical kerosene fuels) and should serve as input to the parametrization.

The parametrization was trained such that the kerosene A350 reference simulations serve as reference case for determining $n_{0,\mathrm{ref}}$ and $n_0^* = n_0/n_{0,\mathrm{ref}}$ (with $N_{0,\mathrm{ref}} = 3.38 \times 10^{12}\,\mathrm{m}^{-1}$ and $b_{\mathrm{span,ref}} = 60.3\,\mathrm{m}$). Note that in particular the m_C values of our A350 setups deviate from the empirical relationship (see Fig. A1 (c) in U2016), and hence, switching to a smaller A320 aircraft gives a smaller n_0 value ($1.29 \times 10^9\,\mathrm{m}^{-3}$ (A350) vs. $8.93 \times 10^8\,\mathrm{m}^{-3}$ (A320)) leading to $n_0^* = 0.69$.

A2 Differences between the original and new parametrization implementation

This section summarizes the differences between the original parametrization provided in Unterstrasser (2016) and the new one presented in Sec. 3.3. The overall design of the parametrization has not changed, and the cookbook of individual computations, as listed in Sec. A6 of U2016, received only minor changes, which are as follows:

- In step 2, the formula for computing the plume area is now $A_\mathrm{p} = 2 \times \pi {r_\mathrm{p}}^2$, which replaces Eq. (A7) of U2016, which was given by $A_\mathrm{p} = 4 \times \pi {r_\mathrm{p}}^2$.
- In step 3, z_atm and z_emit are redefined using now the adiabatic index κ (as given in Eqs. (7) and (8)). Moreover, the bisection method for solving the ~~non-linear~~ nonlinear equation can be replaced by analytically defined fit functions provided in the subsequent subsection.
- In steps 3 and 4, new values for the fitting coefficients are used as given in Eqs. (14a)-(14g). Moreover, the adaptation factor Ψ uses a new definition as given in subsection A1.

The supplement contains Fortran and Python implementations of the new and the original parametrization.

A3 Analytical fit functions of z_{atm} and z_{emit}

To compute the length scales z_{atm} and z_{emit} (Eqs. (7) and (8)), we employed so far the numerical bisection method. Here, we present an alternative approach that directly calculates these length scales based on input data for temperature, ambient supersaturation, and water vapor concentration. The corresponding formulae are as follows:

$$\tilde{z}_{\text{atm}} = 607.46\,\text{m} \times {s_{\text{i}}}^{0.897} \times \left(\frac{T_{\text{CA}}}{205\,\text{K}}\right)^{2.225} \tag{A2}$$

and

$$\tilde{z}_{\text{emit}} = 1106.6\,\text{m} \times \left(\frac{\rho_{\text{emit}}}{10\,\text{mg/m}^3}\right)^{0.678+0.0116\,T_{205}} \times \exp\left((-(0.0807 + 0.000428\,T_{205})\,T_{205})\right) \tag{A3}$$

with $T_{205} = T_{\text{CA}}/\text{K} - 205$.

The resulting length scales show only slight deviations from those derived using the bisection method, with a maximum deviation of 3 m for z_{atm} and 7 m for z_{emit}. Applying the analytical relations to calculate the parametrized survival fraction, we observe no change in 44 % of the data (when rounded to two digits, as done in Tab. A1) and a maximum deviation of 2.0 %. A detailed comparison is provided in Tab. S1. The supplement contains further plots that demonstrate the suitability of the fit functions.

Supplement. The supplement related to this article is available online at:

.

Author contributions. AL performed the simulations, created the tables and figures, and wrote the manuscript with contributions from SU. AL and SU conceptualized the study, evaluated and interpreted the results, and worked on the parametrization extension.

Competing interests. The authors declare that they have no conflict of interest.

Acknowledgements. This work contributes to the DLR-internal projects H2CONTRAIL and H2EAT. Moreover, both authors received funding from Airbus SAS in the framework of understanding contrails from hydrogen propulsion. The authors thank Klaus Gierens ~~for an internal review of the paper draft~~and Charles Renard for feedback on the initial paper draft. They also thank the reviewers for valuable comments. This work used resources of the Deutsches Klimarechenzentrum (DKRZ) granted by its Scientific Steering Committee (WLA) under project ID bd0832.

References

Airbus: Towards the world's first hydrogen-powered commercial aircraft, https://www.airbus.com/en/innovation/energy-transition/hydrogen/zeroe#concepts, 2020.

Airbus: Contrail-chasing Blue Condor makes Airbus' first full hydrogen-powered flight, https://www.airbus.com/en/newsroom/stories/2023-11-contrail-chasing-blue-condor-makes-airbus-first-full-hydrogen-powered#, 2023.

Bier, A. and Burkhardt, U.: Impact of Parametrizing Microphysical Processes in the Jet and Vortex Phase on Contrail Cirrus Properties and Radiative Forcing, J. Geophys. Res., 127, e2022JD036 677, https://doi.org/10.1029/2022JD036677, 2022.

Bier, A., Burkhardt, U., and Bock, L.: Synoptic Control of Contrail Cirrus Life Cycles and Their Modification Due to Reduced Soot Number Emissions, J. Geophys. Res., pp. 11 584–11 603, https://doi.org/10.1002/2017JD027011, 2017JD027011, 2017.

Bier, A., Unterstrasser, S., Zink, J., Hillenbrand, D., Jurkat-Witschas, T., and Lottermoser, A.: Contrail formation on ambient aerosol particles for aircraft with hydrogen combustion: a box model trajectory study, Atmos. Chem. Phys., 24, 2319–2344, https://doi.org/10.5194/acp-24-2319-2024, 2024.

Bräuer, T., Voigt, C., Sauer, D., Kaufmann, S., Hahn, V., Scheibe, M., Schlager, H., Huber, F., Le Clerq, P., Moore, R. H., and Anderson, B. E.: Reduced ice number concentrations in contrails from low-aromatic biofuel blends, Atmos. Chem. Phys., 21, 16 817–16 826, https://doi.org/10.5194/acp-21-16817-2021, 2021.

Burkhardt, U. and Kärcher, B.: Global radiative forcing from contrail cirrus, Nature Clim. Ch., 1, 54–58, https://doi.org/10.1038/nclimate1068, 2011.

Burkhardt, U., Bock, L., and Bier, A.: Mitigating the contrail cirrus climate impact by reducing aircraft soot number emissions, npj Climate and Atmospheric Science, 1, 37, https://doi.org/10.1038/s41612-018-0046-4, 2018.

Clark, T. L. and Farley, R. D.: Severe downslope windstorm calculations in two and three spatial dimensions using anelastic interactive grid nesting: a possible mechanism for gustiness., J. Atmos. Sci., 41, 329–350, 1984.

Crow, S.: Stability theory for a pair of trailing vortices, AIAA Journal, 8, 2172–2179, 1970.

Gierens, K.: Theory of Contrail Formation for Fuel Cells, Aerospace, 8, https://doi.org/10.3390/aerospace8060164, 2021.

Gierens, K. and Spichtinger, P.: On the size distribution of ice-supersaturated regions in the upper troposphere and lowermost stratosphere, Ann. Geophys., 18, 499–504, https://doi.org/10.1007/s00585-000-0499-7, 2000.

Gierens, K., Matthes, S., and Rohs, S.: How Well Can Persistent Contrails Be Predicted?, Aerospace, 7, https://doi.org/10.3390/aerospace7120169, 2020.

Gruber, S., Unterstrasser, S., Bechtold, J., Vogel, H., Jung, M., Pak, H., and Vogel, B.: Contrails and their impact on shortwave radiation and photovoltaic power production – a regional model study, Atmos. Chem. Phys., 18, 6393–6411, https://doi.org/10.5194/acp-18-6393-2018, 2018.

Huebsch, W. and Lewellen, D.: Sensitivity Study on Contrail Evolution, 36 th AIAA Fluid Dynamics Conference and Exhibit,, AIAA 2006-3749, 1–14, https://doi.org/10.2514/6.2006-3749, 2006.

Jansen, J. and Heymsfield, A. J.: Microphysics of Aerodynamic Contrail Formation Processes, J. Atmos. Sci., 72, 3293–3308, https://doi.org/10.1175/JAS-D-14-0362.1, 2015.

Kärcher, B.: Formation and radiative forcing of contrail cirrus, Nature Communications, 9, 1824, https://doi.org/10.1038/s41467-018-04068-0, 2018.

Kärcher, B., Burkhardt, U., Bier, A., Bock, L., and Ford, I. J.: The microphysical pathway to contrail formation, J. Geophys. Res., 120, 7893–7927, https://doi.org/10.1002/2015JD023491, 2015.

Kaufmann, S., Dischl, R., and Voigt, C.: Regional and seasonal impact of hydrogen propulsion systems on potential contrail cirrus cover, Atmos. Environ., 24, 100 298, https://doi.org/10.1016/j.aeaoa.2024.100298, 2024.

Kazula, S., de Graaf, S., and Enghardt, L.: Review of fuel cell technologies and evaluation of their potential and challenges for electrified propulsion systems in commercial aviation, Journal of the Global Power and Propulsion Society, 7, 43–57, https://doi.org/10.33737/jgpps/158036, 2023.

Lee, D. S., Fahey, D. W., Skowron, A., Allen, M. R., Burkhardt, U., Chen, Q., Doherty, S. J., Freeman, S., Forster, P. M., Fuglestvedt, J., Gettelman, A., De León, R. R., Lim, L. L., Lund, M. T., Millar, R. J., Owen, B., Penner, J. E., Pitari, G., Prather, M. J., Sausen, R., and Wilcox, L. J.: The contribution of global aviation to anthropogenic climate forcing for 2000 to 2018, Atmos. Environ., 244, 117 834, https://doi.org/10.1016/j.atmosenv.2020.117834, 2021.

Lee, D. S., Allen, M. R., Cumpsty, N., Owen, B., Shine, K. P., and Skowron, A.: Uncertainties in mitigating aviation non-CO2 emissions for climate and air quality using hydrocarbon fuels, Environ. Sci.: Atmos., 3, 1693–1740, https://doi.org/10.1039/D3EA00091E, 2023.

Lewellen, D. and Lewellen, W.: Large-eddy simulations of the vortex-pair breakup in aircraft wakes, AIAA Journal, 34, 2337–2345, 1996.

Lewellen, D. C.: Persistent contrails and contrail cirrus. Part 2: Full Lifetime Behavior, J. Atmos. Sci., pp. 4420–4438, https://doi.org/10.1175/JAS-D-13-0317.1, 2014.

Lewellen, D. C. and Lewellen, W. S.: Effects of aircraft wake dynamics on measured and simulated NOx and HOx wake chemistry, J. Geophys. Res., 106, 27 661–27 672, 2001.

Lewellen, D. C., Meza, O., and Huebsch, W. W.: Persistent contrails and contrail cirrus. Part 1: Large-eddy simulations from inception to demise, J. Atmos. Sci., 71, 4399–4419, https://doi.org/10.1175/JAS-D-13-0316.1, 2014.

Marciello, V., Di Stasio, M., Ruocco, M., Trifari, V., Nicolosi, F., Meindl, M., Lemoine, B., and Caliandro, P.: Design Exploration for Sustainable Regional Hybrid-Electric Aircraft: A Study Based on Technology Forecasts, Aerospace, 10, https://doi.org/10.3390/aerospace10020165, 2023.

Märkl, R. S., Voigt, C., Sauer, D., Dischl, R. K., Kaufmann, S., Harlaß, T., Hahn, V., Roiger, A., Weiß-Rehm, C., Burkhardt, U., Schumann, U., Marsing, A., Scheibe, M., Dörnbrack, A., Renard, C., Gauthier, M., Swann, P., Madden, P., Luff, D., Sallinen, R., Schripp, T., and Le Clercq, P.: Powering aircraft with 100 % sustainable aviation fuel reduces ice crystals in contrails, Atmos. Chem. Phys., 24, 3813–3837, https://doi.org/10.5194/acp-24-3813-2024, 2024.

Marks, T., Dahlmann, K., Grewe, V., Gollnick, V., Linke, F., Matthes, S., Stumpf, E., Swaid, M., Unterstrasser, S., Yamashita, H., and Zumegen, C.: Climate Impact Mitigation Potential of Formation Flight, Aerospace, 8, 14, https://doi.org/10.3390/aerospace8010014, 2021.

Moore, R. H., Thornhill, K. L., Weinzierl, B., Sauer, D., D'Ascoli, E., Kim, J., Lichtenstern, M., Scheibe, M., Beaton, B., Beyersdorf, A. J., Barrick, J., Bulzan, D., Corr, C. A., Crosbie, E., Jurkat, T., Martin, R., Riddick, D., Shook, M., Slover, G., Voigt, C., White, R., Winstead, E., Yasky, R., Ziemba, L. D., Brown, A., Schlager, H., and Anderson, B. E.: Biofuel blending reduces particle emissions from aircraft engines at cruise conditions, Nature, 543, 411–415, https://doi.org/10.1038/nature21420, 2017.

Petzold, A., Kramer, M., Neis, P., Rolf, C., Rohs, S., Berkes, F., Smit, H. G. J., Gallagher, M., Beswick, K., Lloyd, G., Baumgardner, D., Spichtinger, P., Nedelec, P., Ebert, V., Buchholz, B., Riese, M., and Wahner, A.: Upper tropospheric water vapour and its interaction with cirrus clouds as seen from IAGOS long-term routine in situ observations, Faraday Discuss., 200, 229–249, https://doi.org/10.1039/C7FD00006E, 2017.

Picot, J., Paoli, R., Thouron, O., and Cariolle, D.: Large-eddy simulation of contrail evolution in the vortex phase and its interaction with atmospheric turbulence, Atmos. Chem. Phys., 15, 7369–7389, https://doi.org/10.5194/acp-15-7369-2015, 2015.

Ponsonby, J., King, L., Murray, B. J., and Stettler, M. E. J.: Jet aircraft lubrication oil droplets as contrail ice-forming particles, Atmos. Chem. Phys., 24, 2045–2058, https://doi.org/10.5194/acp-24-2045-2024, 2024.

Prusa, J., Smolarkiewicz, P., and Wyszogrodzki, A.: EULAG, a computational model for multiscale flows, Comput. Fluids, 37, 1193–1207, https://doi.org/10.1016/j.compfluid.2007.12.001, 2008.

Schumann, U.: On conditions for contrail formation from aircraft exhausts, Meteorol. Z., 5, 4–23, https://doi.org/10.1127/metz/5/1996/4, 1996.

Schumann, U., Mayer, B., Gierens, K., Unterstrasser, S., Jessberger, P., Petzold, A., Voigt, C., and Gayet, J.-F.: Effective Radius of Ice Particles in Cirrus and Contrails, J. Atmos. Sci., 68, 300–321, https://doi.org/10.1175/2010JAS3562.1, 2011.

Smolarkiewicz, P. and Margolin, L.: On forward-in-time differencing for fluids: an Eulerian/semi-Lagrangian non-hydrostatic model for stratified flows, Atmosphere-Ocean Special, 35, 127–152, 1997.

Sölch, I. and Kärcher, B.: A large-eddy model for cirrus clouds with explicit aerosol and ice microphysics and Lagrangian ice particle tracking, Q. J. R. Meteorol. Soc., 136, 2074–2093, https://doi.org/10.1002/qj.689, 2010.

Sussmann, R. and Gierens, K.: Lidar and numerical studies on the different evolution of vortex pair and secondary wake in young contrails, J. Geophys. Res., 104, 2131–2142, 1999.

Tiwari, S., Pekris, M. J., and Doherty, J. J.: A review of liquid hydrogen aircraft and propulsion technologies, International Journal of Hydrogen Energy, 57, 1174–1196, https://doi.org/10.1016/j.ijhydene.2023.12.263, 2024.

Ungeheuer, F., van Pinxteren, D., and Vogel, A. L.: Identification and source attribution of organic compounds in ultrafine particles near Frankfurt International Airport, Atmos. Chem. Phys., 21, 3763–3775, https://doi.org/10.5194/acp-21-3763-2021, 2021.

Ungeheuer, F., Caudillo, L., Ditas, F., Simon, M., van Pinxteren, D., Kilic, D., Rose, D., Jacobi, S., Kürten, A., Curtius, J., and Vogel, A. L.: Nucleation of jet engine oil vapours is a large source of aviation-related ultrafine particles, Commun. Earth Environ., 3, 1–8, https://doi.org/10.1038/s43247-022-006, 2022.

Unterstrasser, S.: Large eddy simulation study of contrail microphysics and geometry during the vortex phase and consequences on contrail-to-cirrus transition, J. Geophys. Res., 119, 7537–7555, https://doi.org/10.1002/2013JD021418, 2014.

Unterstrasser, S.: Properties of young contrails - a parametrisation based on large-eddy simulations, Atmos. Chem. Phys., 16, 2059–2082, https://doi.org/10.5194/acp-16-2059-2016, 2016.

Unterstrasser, S.: The Contrail Mitigation Potential of Aircraft Formation Flight Derived from High-Resolution Simulations, Aerospace, 7, 170, https://doi.org/10.3390/aerospace7120170, 2020.

Unterstrasser, S. and Gierens, K.: Numerical simulations of contrail-to-cirrus transition - Part 2: Impact of initial ice crystal number, radiation, stratification, secondary nucleation and layer depth, Atmos. Chem. Phys., 10, 2037–2051, https://doi.org/10.5194/acp-10-2037-2010, 2010.

Unterstrasser, S. and Görsch, N.: Aircraft-type dependency of contrail evolution, J. Geophys. Res., 119, 14,015–14,027, https://doi.org/10.1002/2014JD022642, 2014.

Unterstrasser, S. and Sölch, I.: Study of contrail microphysics in the vortex phase with a Lagrangian particle tracking model, Atmos. Chem. Phys., 10, 10 003–10 015, https://doi.org/10.5194/acp-10-10003-2010, 2010.

Unterstrasser, S. and Stephan, A.: Far field wake vortex evolution of two aircraft formation flight and implications on young contrails, Aeronaut. J., 124, 667–702, https://doi.org/10.1017/aer.2020.3, 2020.

Unterstrasser, S., Paoli, R., Sölch, I., Kühnlein, C., and Gerz, T.: Dimension of aircraft exhaust plumes at cruise conditions: effect of wake vortices, Atmos. Chem. Phys., 14, 2713–2733, https://doi.org/10.5194/acp-14-2713-2014, 2014.

Unterstrasser, S., Gierens, K., Sölch, I., and Lainer, M.: Numerical simulations of homogeneously nucleated natural cirrus and contrail-cirrus. Part 1: How different are they?, Meteorol. Z., 26, 621–642, https://doi.org/10.1127/metz/2016/0777, 2017a.

Unterstrasser, S., Gierens, K., Sölch, I., and Wirth, M.: Numerical simulations of homogeneously nucleated natural cirrus and contrail-cirrus. Part 2: Interaction on local scale, Meteorol. Z., 26, 643–661, https://doi.org/10.1127/metz/2016/0780, 2017b.

Voigt, C., Kleine, J., Sauer, D., Moore, R. H., Bräuer, T., Le Clercq, P., Kaufmann, S., Scheibe, M., Jurkat-Witschas, T., Aigner, M., Bauder, U., Boose, Y., Borrmann, S., Crosbie, E., Diskin, G. S., DiGangi, J., Hahn, V., Heckl, C., Huber, F., Nowak, J. B., Rapp, M., Rauch, B., Robinson, C., Schripp, T., Shook, M., Winstead, E., Ziemba, L., Schlager, H., and Anderson, B. E.: Cleaner burning aviation fuels can reduce contrail cloudiness, Commun. Earth Environ., 2, 114, https://doi.org/10.1038/s43247-021-00174-y, 2021.

Wölk, J. and Strey, R.: Homogeneous Nucleation of H2O and D2O in Comparison: The Isotope Effect, The Journal of Physical Chemistry B, 105, 11 683–11 701, https://doi.org/10.1021/jp0115805, 2001.

Yu, F., Kärcher, B., and Anderson, B. E.: Revisiting Contrail Ice Formation: Impact of Primary Soot Particle Sizes and Contribution of Volatile Particles, Environ. Sci. Technol., 58, 17 650–17 660, https://doi.org/10.1021/acs.est.4c04340, 2024.

Nr	AC	~~T_{amb}~~ T_{CA} (K)	$RH_{\mathrm{i,amb}}$ (%)	N_{BV} ($10^{-2}\,\mathrm{s}^{-1}$)	N_0 #sim	I_0 ($\mathrm{g\,m}^{-1}$)	r_{SD}	$f_{N,\mathrm{s}}$	$\hat{f}_{N,\mathrm{s}}$	z_{atm} (m)	z_{emit} (m)	$\hat{z}_{\mathrm{desc}}$ (m)
1,2,3,4,5	A350	217	120	1.15	5	15.0	3.0	0.05, 0.23, 0.65, 0.89, 0.98	0.06, 0.23, 0.6, 0.87, 0.97	164	249	339
6,7,8,9,10	A350	217	110	1.15	5	15.0	3.0	0.02, 0.1, 0.28, 0.46, 0.71	0.0, 0.06, 0.22, 0.58, 0.86	85	249	339
11,12,13,14,15,16	A350	217	120	1.15	6	38.55	3.0	0.02, 0.09, 0.39, 0.85, 0.98, 1.0	0.05, 0.2, 0.57, 0.85, 0.96, 1.0	164	546	339
17,18,19,20,21	A350	217	110	1.15	5	38.55	3.0	0.07, 0.27, 0.63, 0.81, 0.92	0.08, 0.29, 0.68, 0.9, 0.98	85	546	339
22,23,24	A350	217	120	1.15	3	15.0	1.0	0.07, 0.88, 1.0	0.06, 0.6, 0.97	164	249	339
25,26,27	A350	217	120	1.15	3	15.0	4.0	0.05, 0.61, 0.98	0.06, 0.6, 0.97	164	249	339
28,29,30	A350	217	110	1.15	3	15.0	1.0	0.05, 0.49, 0.93	0.0, 0.21, 0.86	85	249	339
31,32,33	A350	217	110	1.15	3	15.0	4.0	0.02, 0.26, 0.67	0.0, 0.22, 0.86	85	249	339
34,35,36	A350	217	120	1.15	3	38.55	1.0	0.18, 1.0, 1.0	0.2, 0.85, 1.0	164	546	339
37,38,39	A350	217	120	1.15	3	38.55	4.0	0.09, 0.81, 0.99	0.2, 0.85, 1.0	164	546	339
40,41,42	A350	217	110	1.15	3	38.55	1.0	0.18, 0.92, 1.0	0.08, 0.68, 0.98	85	546	339
43,44,45	A350	217	110	1.15	3	38.55	4.0	0.06, 0.58, 0.89	0.08, 0.68, 0.98	85	546	339
46,47,48	A350	217	120	0.5	3	15.0	3.0	0.02, 0.28, 0.66	0.0, 0.26, 0.94	164	249	515
49,50,51	A350	217	110	0.5	3	15.0	3.0	0.01, 0.1, 0.31	0.0, 0.02, 0.73	85	249	515
52,53,54	A350	217	120	0.5	3	38.55	3.0	0.04, 0.46, 0.84	0.02, 0.71, 1.0	164	546	515
55,56,57	A350	217	110	0.5	3	38.55	3.0	0.02, 0.26, 0.53	0.0, 0.36, 0.96	85	546	515
Simulations at higher ambient temperatures												
58,59,60,61,62	A350	225	120	1.15	5	15.0	3.0	0.02, 0.12, 0.45, 0.76, 0.95	0.03, 0.14, 0.44, 0.79, 0.94	177	110	339
63,64,65,66,67	A350	225	110	1.15	5	15.0	3.0	0.01, 0.04, 0.13, 0.25, 0.45	0.0, 0.01, 0.09, 0.3, 0.69	92	110	339
68,69,70,71,72	A350	225	120	1.15	5	38.55	3.0	0.04, 0.21, 0.63, 0.9, 0.99	0.08, 0.28, 0.67, 0.9, 0.98	177	262	339
73,74,75,76,77	A350	225	110	1.15	5	38.55	3.0	0.02, 0.1, 0.29, 0.46, 0.68	0.0, 0.07, 0.27, 0.65, 0.89	92	262	339
78,79,80,81,82	A350	230	120	1.15	5	38.55	3.0	0.03, 0.15, 0.51, 0.83, 0.97	0.05, 0.21, 0.57, 0.86, 0.97	186	163	339
83,84,85,86,87	A350	230	110	1.15	5	38.55	3.0	0.01, 0.05, 0.17, 0.31, 0.52	0.0, 0.03, 0.15, 0.46, 0.81	97	163	339
88,89,90,91,92	A350	233	120	1.15	5	38.55	3.0	0.02, 0.12, 0.45, 0.78, 0.97	0.05, 0.19, 0.53, 0.84, 0.96	191	123	339
93,94,95,96,97	A350	233	110	1.15	5	38.55	3.0	0.01, 0.04, 0.14, 0.26, 0.45	0.0, 0.02, 0.12, 0.38, 0.76	99	123	339
98,99,100	A350	233	120	1.15	3	38.55	1.0	0.03, 0.63, 1.0	0.04, 0.53, 0.96	191	123	339
101,102,103	A350	233	120	1.15	3	38.55	4.0	0.02, 0.43, 0.96	0.05, 0.53, 0.96	191	123	339
104,105,106	A350	233	110	1.15	3	38.55	1.0	0.01, 0.25, 0.59	0.0, 0.12, 0.76	99	123	339
107,108,109	A350	233	110	1.15	3	38.55	4.0	0.01, 0.12, 0.43	0.0, 0.12, 0.76	99	123	339
110,111,112,113,114	A350	235	120	1.15	5	38.55	3.0	0.02, 0.11, 0.43, 0.75, 0.95	0.04, 0.18, 0.52, 0.83, 0.96	195	102	339
115,116,117,118,119	A350	235	110	1.15	5	38.55	3.0	0.01, 0.03, 0.12, 0.23, 0.42	0.0, 0.01, 0.1, 0.34, 0.73	101	102	339
Simulations with A320/B737-like aircraft												
120	A320	217	120	1.15	1	3.7	3.0	0.89	0.72	164	176	231
121,122,123	A320	225	120	1.15	3	3.7	3.0	0.05, 0.78, 1.0	0.13, 0.64, 0.96	177	76	231
124,125,126	A320	225	110	1.15	3	3.7	3.0	0.01, 0.29, 0.86	0.03, 0.21, 0.78	92	76	231
127,128,129	A320	225	120	1.15	3	9.51	3.0	0.07, 0.85, 1.0	0.2, 0.76, 0.99	177	185	231
130,131,132	A320	225	110	1.15	3	9.51	3.0	0.03, 0.52, 0.96	0.07, 0.39, 0.9	92	185	231
133,134,135	A320	230	120	1.15	3	9.51	3.0	0.05, 0.8, 1.0	0.17, 0.72, 0.98	186	114	231
136,137,138	A320	230	120	1.15	3	9.51	3.0	0.02, 0.35, 0.88	0.04, 0.29, 0.85	186	114	231
139,140,141	A320	233	120	1.15	3	9.51	3.0	0.04, 0.78, 1.0	0.16, 0.71, 0.97	191	85	231
142,143,144	A320	233	110	1.15	3	9.51	3.0	0.01, 0.3, 0.86	0.04, 0.26, 0.82	99	85	231
145,146,147	A320	235	120	1.15	3	9.51	3.0	0.04, 0.76, 1.0	0.16, 0.7, 0.97	195	70	231
148,149,150	A320	235	110	1.15	3	9.51	3.0	0.01, 0.27, 0.84	0.03, 0.24, 0.81	101	70	231

Table A1. Summary of the simulations performed. Columns ~~2~~3–5 list the meteorological parameters, while columns 6-8 present the microphysical initialization settings. Columns ~~8 and~~ 9 and 10 display both the simulated and parametrized survival fractions. Lastly, columns ~~10-12~~ 11-13 specify the length scales employed in the parametrization. Rows displaying five simulations correspond to sets with N_0-scaling factors of 100, 10, 1, 0.1, and 0.01. Rows showing three simulations represent sets with scaling factors of 100, 1, and 0.01. In the third row, a total of six simulations are included, with simulation 11 performed using a scaling factor of 1000.

Supplementary material to manuscript "High-resolution modelling of early contrail evolution from hydrogen-powered aircraft"

Annemarie Lottermoser and Simon Unterstrasser

Deutsches Zentrum für Luft- und Raumfahrt, Institut für Physik der Atmosphäre, Oberpfaffenhofen, Germany

Correspondence: Annemarie Lottermoser (annemarie.lottermoser@dlr.de)

1 ~~Evaluation~~ Temporal and spatial evolution of ~~z_{atm}~~ temperature and ~~z_{emit}~~ ~~In the ice~~ humidity during the vortex phase

Figure S1 illustrates the evolution of ice relative humidity (a) and temperature difference (b), where the background temperature profile has been subtracted. Within the wake vortices, the ice relative humidity remains close to saturation until the vortices dissipate. This phenomenon results from the sublimation of ice crystals trapped in the primary wake. The sublimation increases the local water vapor concentration, balancing the decrease in RH_{i} caused by adiabatic heating. Note that humidity values below 100 % may occur as the sublimation does not instantaneously relax the humidity field to saturation. In the secondary wake, RH_{i} also remains near saturation as detrained ice crystals deplete ambient moisture, reducing the environmental supersaturation toward saturation. The presented humidity fields are quite smooth as they are averages along flight direction.

Initially, the temperature perturbation is nearly everywhere close to zero. The centers of the wake vortices feature a pressure drop to compensate for centrifugal forces and can lead to a very localized temperature drop. Due to the prescribed stable stratification, air masses at the original flight altitude have a higher potential temperature than air masses beneath. Hence, the descending primary wake is identified by positive ΔT values. A similar consideration explains the negative ΔT values after six minutes around $z = 0\,\text{m}$. Air masses from the primary wake rise back to the initial altitude and push or contain also air masses from lower altitudes (with lower potential temperature) to $z = 0\,\text{m}$ leading to $\Delta T < 0\,\text{K}$.

2 Further information on ice crystal loss parametrization

2.1 Evaluation of z_{atm} and z_{emit}

In the ice crystal loss parametrization, the two length scales z_{atm} and z_{emit} are implicitly defined. In the original version in U2016 (= Unterstrasser, 2016), the non-linear equations were solved using a numerical method (classical bisection method). To speed up evaluations and to provide explicit formulations, fit formulae for the two length scales z_{atm} and z_{emit} were derived as outlined in Sec. (A3) of this study. In order to compare both versions simulation-wise, the length scale values determined with the bisection method and the fit formulae are compared. Moreover, the corresponding survival fractions based on either evaluation method are calculated. The outcomes are provided in Tab. S1. As ~~already summarized~~ noted in the main text~~of the~~

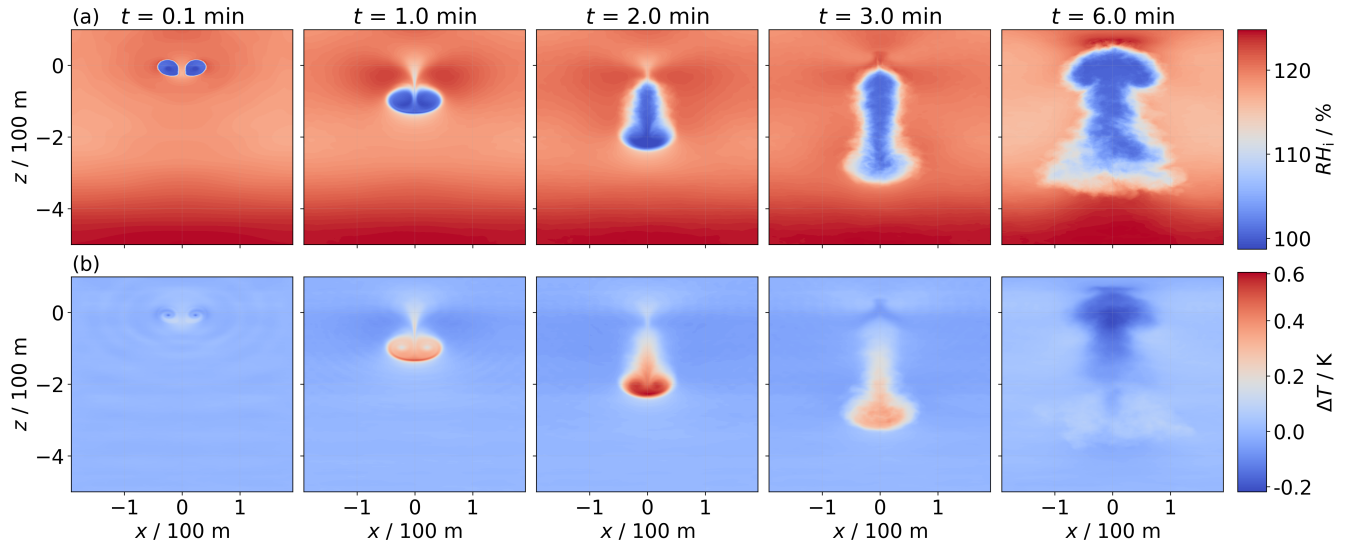

Figure S1. Temporal evolution of relative humidity with respect to ice (a) and temperature difference (b) in the x, z-plane (averaged along flight direction). In (b), the vertical background temperature profile is subtracted to highlight the temperature evolution, particularly within the primary wake. Note that the first column corresponds to 0.1 min, whereas the zeroth time step is shown in the main body of the manuscript. This distinction is made because the thermodynamic fields exhibit almost no visible features at the initial time step. The depicted exemplary simulation is performed for an A350/B777-like aircraft at $T_{\mathrm{CA}} = 217\,\mathrm{K}$, $RH_{\mathrm{i,amb}} = 120\,\%$, $N_{\mathrm{BV}} = 1.5 \times 10^{-2}\,\mathrm{s}^{-1}$, $N_0 = 3.38 \times 10^{12}\,\mathrm{m}^{-1}$, $I_0 = 15.0\,\mathrm{g\,m}^{-1}$, and $r_{\mathrm{SD}} = 3.0$.

~~present study: "Applying the~~ , applying the analytical relations to ~~calculate~~ compute the parametrized survival fraction ~~, we observe no change in~~ yields no change for 44 % of the data points (~~when~~ rounded to two ~~digits, as done~~ decimal places, as in Tab. A1)~~and a maximum deviation of~~ , and the maximum deviation observed is 2.0 %. ~~A detailed comparison is provided in Tab. S1."~~

3 ~~Comparison of the original and new ice crystal loss parametrization~~

2.1 Comparison of the original and new ice crystal loss parametrization

The original ice crystal loss parametrization proposed in U2016 has been implemented in several larger-scale contrail models to refine the contrail initialization in those models (Gruber et al., 2018; Bier and Burkhardt, 2022), and applications were confined to conventional kerosene contrails.

This section presents comparison plots between the original and updated version of the ice crystal loss parametrization. Figure S2 shows scatter plots of z_Δ (panel (a)) and the parametrized survival fraction $\hat{f}_{N,\mathrm{s}}$ (panel (b)), with the x-axis representing the original (2016) values and the y-axis showing the updated (2025) data. The values of z_Δ are similar across both formulations, although $z_{\Delta,2025}$ is generally slightly lower. However, differences in z_Δ should not be over-interpreted as this

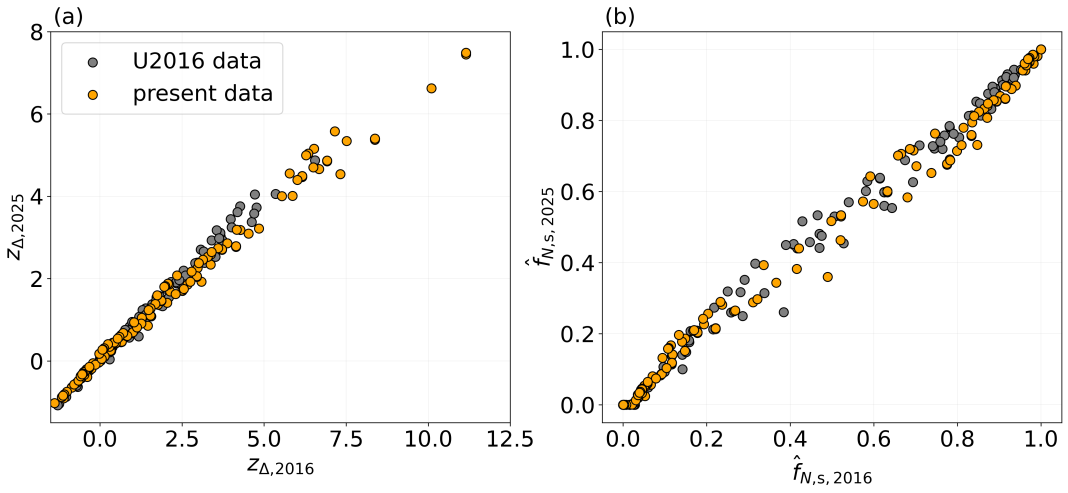

Figure S2. Scatter plot comparing the 2016 z_Δ values with the z_Δ values from the present study (a), and a similar comparison for the parametrized survival fractions (b).

quantity serves as argument in an arctan-type function (see Eq. (12)) to retrieve the survival fraction. The arctan-type function formulation includes three fit coefficients that change from one to the other version. Hence, panel (b) shows the eventual differences in the parametrized survival fraction from the two versions. Likewise, $\hat{f}_{N,\mathrm{s}}$ exhibits only minor scatter between the two versions.

Furthermore, we reproduce plots that were shown in U2016 (Figs. 5, 9, and 10 in that publication). In the new versions of those plots (Figs. S3-S5 in this document), we juxtapose the outcome of the original and the new parametrization. This should demonstrate that the switch to the new formulation has only marginal implications on applications focusing on conventional kerosene contrails.

3 Sensitivity analyses: Numerical and physical aspects

In the following, three sensitivity studies are presented. We compare the results of a reference simulation, performed for an A350/B777-like aircraft at $T_{\mathrm{CA}} = 217\,\mathrm{K}$, $RH_{\mathrm{i,amb}} = 120\,\%$, $N_{\mathrm{BV}} = 1.5 \times 10^{-2}\,\mathrm{s}^{-1}$, $N_0 = 3.38 \times 10^{12}\,\mathrm{m}^{-1}$, $I_0 = 15.0\,\mathrm{g\,m}^{-1}$, and $r_{\mathrm{SD}} = 3.0$ (solid black lines in Fig. S6). These are compared to simulations in which the grid resolution, domain size, and ambient pressure are varied individually.

3.1 Impact of grid resolution

In the reference setup, we employ a horizontal and vertical grid spacing of 1 m. To assess the sensitivity of contrail evolution to mesh resolution, we conduct an additional simulation using a finer resolution of 0.5 m. As shown by the magenta curves in Fig. S6, the higher-resolution simulation results in a relative increase of 7.7 % in total ice mass and a reduction in ice

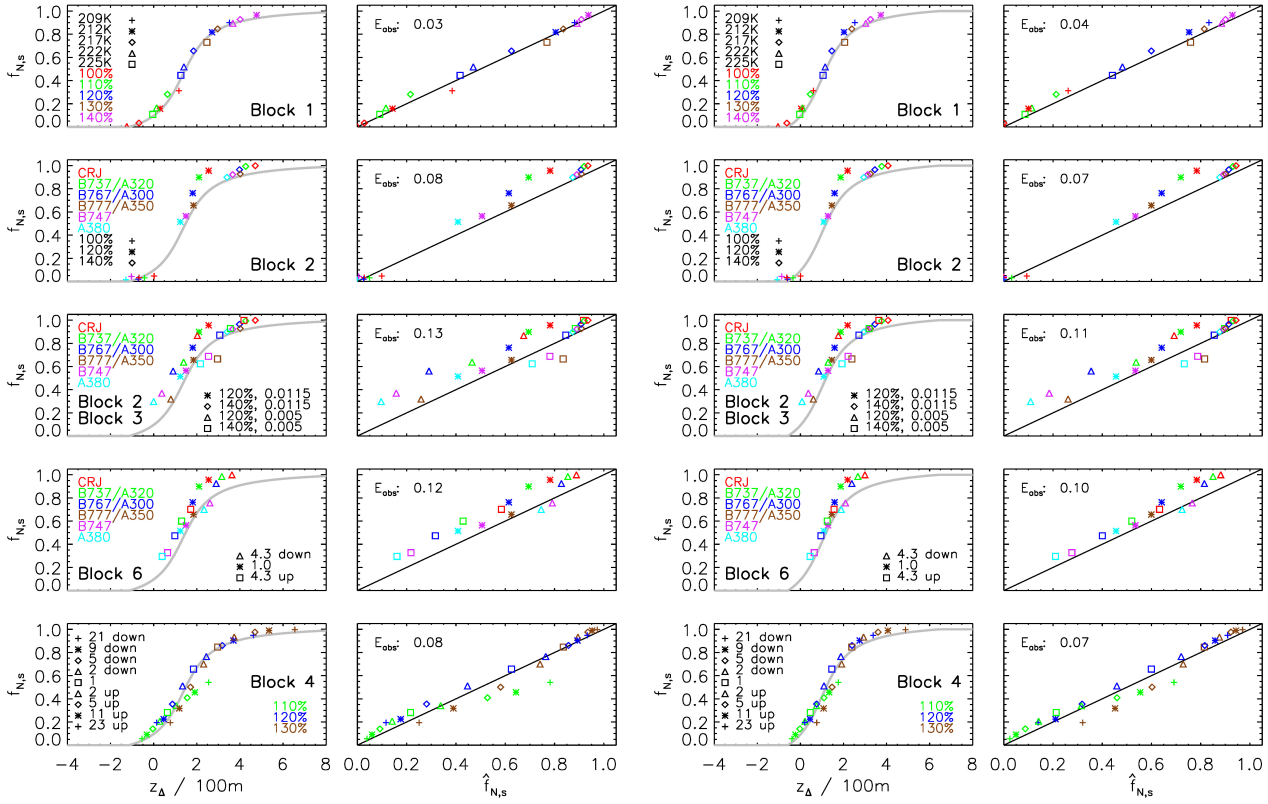

Figure S3. Reproduced version of Fig. 5 in U2016. The first two columns show the original plot from U2016. The third and fourth ~~column~~ columns use the parametrized survival fractions as obtained from the new parametrization version described in the present study.

Adapted figure caption of U2016:

Columns 1 and 3: Relationship between simulated survival fraction $f_{N,s}$ and z_Δ. The grey curve shows the fit function ~~$\hat{a}$~~ $\hat{a}(z_\Delta)$ as defined in Eq. (12) in the present study.

Columns 2 and 4: Relationship between simulated survival fraction $f_{N,s}$ and approximated survival fraction $\hat{f}_{N,s}$. The black line shows the one-to-one line. Each row shows a subset of simulations taken from various simulation blocks defined in Table A2 of U2016. For example, the first row shows simulations of block 1, where RH_i and T_{CA} are varied. The legend in the plot provides a list of the symbols and colors, which uniquely ~~define~~ defines the ~~simulations~~ simulation parameters of each plotted data point. The root mean square of the absolute error $\hat{f}_{N,s} - f_{N,s}$ is denoted as E_{abs} and given for each subset.

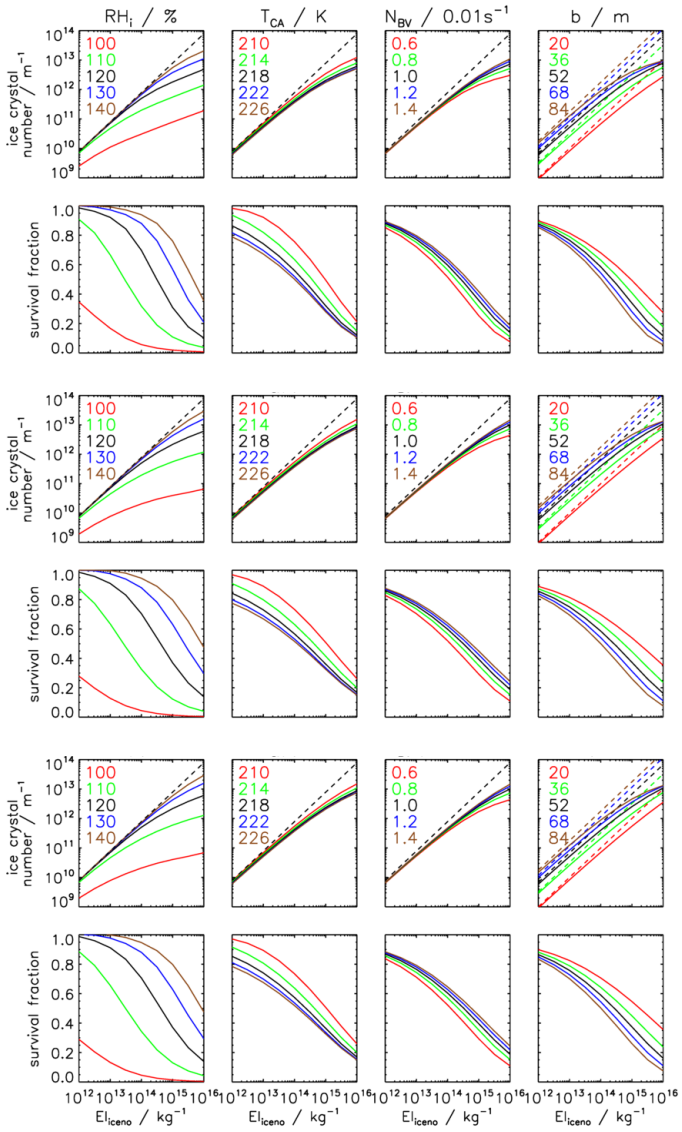

Figure S4. Reproduced version of Fig. 9 in U2016. The first two rows show the original plot from U2016. The other rows use the parametrized survival fractions as obtained from the new parametrization version described in the present study evaluating z_{atm} and z_{emit} either via bisection (rows 3 &and 4) or by employing the fit functions (rows 5 &and 6).

Adapted figure caption of U2016:

Sensitivity of ice crystal loss to EI_{iceno} for various values of RH_i, T, N_{BV}, and b (from left to right). See legend for the color coding. Rows 1, 3, and 5: Ice crystal number per meter of flight path before and after the vortex phase (dashed and solid curves). Note that the initial ice crystal number depends only on b and EI_{iceno} (following Eq. (A10) in U2016, which assumes a water vapor emission index of 1.25–kg/kg). Hence, only one dashed curve is shown in the columns for RH_i, T, and N_{BV}, respectively. Rows 2, 4, and 6: Survival fraction.

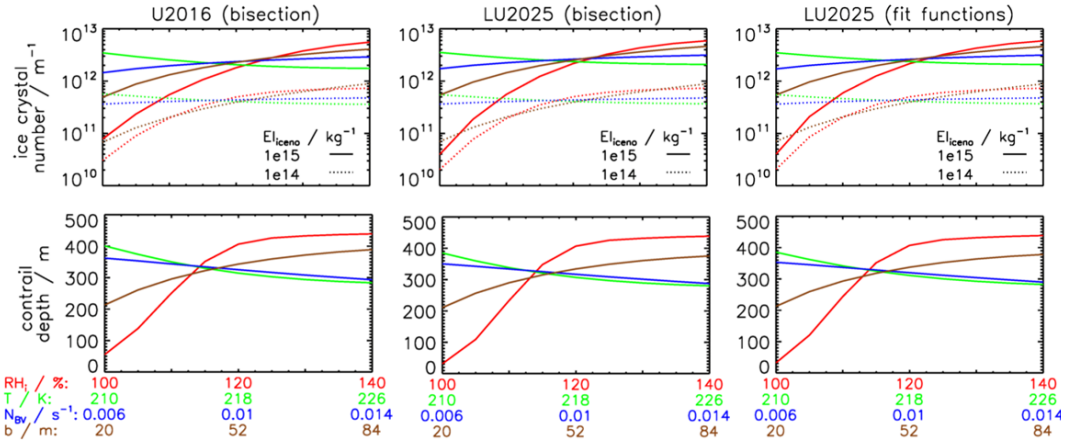

Figure S5. Reproduced version of Fig. 10 in U2016. The first column ~~show~~ shows the original plot from U2016. The two other columns use the new parametrization version (for both types of z_{atm} and z_{emit}).

Adapted figure caption of U2016:

Ice crystal number per meter of flight path (top) and contrail depth (bottom) after the vortex phase as a function of RH_i, T, N_{BV}, or b. EI_{iceno} is ~~10^{15}~~ 10^{15} or ~~10^{14}~~ 10^{14} kg^{-1}. The contrail depth parametrization does not depend on EI_{iceno}. Note that the parametrization of the contrail depth H was not updated in the present study. The slightly different results come from the fact that the parametrization of H uses the parametrized $f_{N,s}$ value as input. Note that the original plot in U2016 showed an additional panel with ice crystal number concentrations, which is left out here.

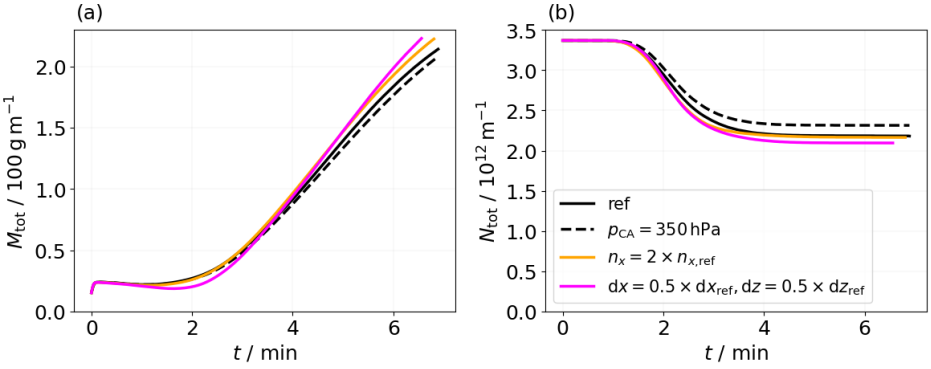

Figure S6. Evolution of total ice crystal number (a) and total ice mass (b) for the reference case and three sensitivity simulations, differentiated by color and line style. The dashed black curves represent a simulation conducted at a higher ambient pressure value. The orange curves correspond to a simulation with doubled domain width. The magenta curves show the results from a simulation with a higher mesh resolution in transverse and vertical direction.

crystal survival fraction from 64.7 % to 62.1 %. Vertical profiles of ice crystal number and mass (not shown) indicate that, in the high-resolution setup, fewer ice crystals are detrained from the vortex system. Instead, a larger fraction remains trapped within the primary wake, where they are more prone to sublimation due to adiabatic heating. The reduced detrainment can be attributed to the way secondary vorticity, generated by baroclinic torque arising from density and pressure gradients between the wake and the ambient air (Holzäpfel et al., 2001), develops in the simulation. Although the underlying physical conditions, such as pressure and density gradients, remain unchanged, the finer grid spacing enables a more accurate resolution of these instabilities, potentially altering the dynamics of vortex destabilization. We hypothesize that the improved representation of secondary vorticity results in less disruption of the vortex cores, thereby reducing ice crystal detrainment and increasing sublimation within the primary wake. Alongside this physical explanation of the observed results, we note that background turbulence could likewise influence the detrainment process and contribute to the observed behavior. While the resulting discrepancies in ice crystal number and mass are moderate compared to those induced by variations in the initial ice crystal number, they underscore the relevance of mesh resolution and its potential impact on simulation outcomes. However, in the context of a sensitivity study focused on variations in initial ice crystal number, where ice crystal survival fractions span the full range from 0 to 100 %, we consider deviations in ice crystal survival fraction below 3 % to be minor. Given the substantial computational demands of finer mesh resolutions (roughly eight times higher CPU time) and considering the comparatively minor differences in simulation outcomes, we consider the baseline resolution appropriate for the objectives of this study.

3.2 Impact of domain size

The default domain size in the transverse direction is 384 grid boxes, corresponding to 384 m in our reference A350/B777 simulation with a grid spacing of $\mathrm{d}x = 1\,\mathrm{m}$. In a sensitivity simulation, we increase the domain width from 384 m to 768 m; the results are shown as orange curves in Fig. S6. This modification yields a slight reduction in final ice crystal survival fraction from 64.7 % to 64.2 % and a relative increase of 4.6 % in final ice mass. A plausible explanation is that, in the narrower domain, the descending vortex pairs might interact across the transverse boundaries, damping their descent and thereby enhancing ice crystal survival. Horizontal profiles reveal that, from about two minutes onward, the wider-domain simulation exhibits slightly lower ice crystal number and mass near the outer edges of the vortices, while more ice crystals and ice mass are found in the vortex centers. This supports the hypothesis that transverse interactions across the boundaries in the narrow domain might influence vortex dynamics and particle motion. However, it is equally plausible that the minor deviations in the evolution of ice crystal number and mass reflect variability introduced by background turbulence, as discussed in the previous section. As the wider domain has a negligible effect on the contrail properties, most notably the ice crystal survival fraction, yet significantly increases computational expense, a transverse width of 384 grid boxes is deemed sufficient for our simulations.

3.3 Impact of pressure variation

A variation of the ambient pressure value has only minor impact on the evolution of ice crystal mass and number, see black dashed curves in Fig. S6. The pressure at flight altitude of the reference simulation is 231 hPa. We increase the pressure to 350 hPa, keeping all other setup parameters (specifically ambient temperature) unchanged. We observe a slightly reduced

final ice mass and a slightly increased number of surviving ice crystals in the higher-pressure case. These differences can be primarily attributed to the pressure dependence of water vapor diffusivity, which appears in the governing equation for ice mass growth (Sölch and Kärcher, 2010). Since diffusivity is inversely proportional to pressure, higher ambient pressure leads to lower diffusivity, thereby reducing the rate of ice crystal growth. Conversely, sublimation is also reduced under higher pressure for the same reason, leading to a slightly higher survival fraction. An additional, though secondary, factor is the pressure dependence of sedimentation velocity. Increased pressure results in a small reduction in sedimentation velocity. However, for a pressure increase of 120 hPa, the resulting change in sedimentation velocity is on the order of 0.5 %, and is thus considered negligible in this context. Overall, the sensitivity of contrail evolution to ambient pressure variations is weak. The final ice crystal survival fraction changes from 64.7 % to 68.7 %, and the total ice mass differs relatively by 4.0 %. This limited sensitivity is expected: the amount of available atmospheric water vapor, expressed in terms of water vapor concentration $\rho_{\mathrm{WV,avail}} = (RH_{\mathrm{i,amb}} - 1) \times \rho_{\mathrm{WV,sat,ice}} = (RH_{\mathrm{i,amb}} - 1) \times \frac{e_s(T)}{R_{\mathrm{WV}} T}$, is primarily temperature-dependent and independent of ambient pressure. Moreover, the adiabatic heating in the descending vortex pair does not depend on ambient pressure.

References

Bier, A. and Burkhardt, U.: Impact of Parametrizing Microphysical Processes in the Jet and Vortex Phase on Contrail Cirrus Properties and Radiative Forcing, J. Geophys. Res., 127, e2022JD036 677, https://doi.org/10.1029/2022JD036677, 2022.

Gruber, S., Unterstrasser, S., Bechtold, J., Vogel, H., Jung, M., Pak, H., and Vogel, B.: Contrails and their impact on shortwave radiation and photovoltaic power production – a regional model study, Atmos. Chem. Phys., 18, 6393–6411, https://doi.org/10.5194/acp-18-6393-2018, 2018.

Holzäpfel, F., Gerz, T., and Baumann, R.: The turbulent decay of trailing vortex pairs in stably stratified environments, Aerosp. Sci. Technol., 5, 95–108, 2001.

Sölch, I. and Kärcher, B.: A large-eddy model for cirrus clouds with explicit aerosol and ice microphysics and Lagrangian ice particle tracking, Q. J. R. Meteorol. Soc., 136, 2074–2093, https://doi.org/10.1002/qj.689, 2010.

Unterstrasser, S.: Properties of young contrails - a parametrisation based on large-eddy simulations, Atmos. Chem. Phys., 16, 2059–2082, https://doi.org/10.5194/acp-16-2059-2016, 2016.

Nr	$\hat{f}_{N,\mathrm{s}}$	$\tilde{f}_{N,\mathrm{s}}$	z_{atm}	$\tilde{z}_{\mathrm{atm}}$ / m	z_{emit} / m	$\tilde{z}_{\mathrm{emit}}$ / m
1,2,3,4,5	0.06, 0.23, 0.6, 0.87, 0.97	0.05, 0.21, 0.59, 0.87, 0.98	164	163	249	250
6,7,8,9,10	0.0, 0.06, 0.22, 0.58, 0.86	0.0, 0.05, 0.22, 0.59, 0.87	85	87	249	250
11,12,13,14,15,16	0.05, 0.2, 0.57, 0.85, 0.96, 1.0	0.05, 0.19, 0.55, 0.86, 0.97, 1.0	164	163	546	541
17,18,19,20,21	0.08, 0.29, 0.68, 0.9, 0.98	0.08, 0.28, 0.68, 0.91, 0.99	85	87	546	541
22,23,24	0.06, 0.6, 0.97	0.05, 0.59, 0.98	164	163	249	250
25,26,27	0.06, 0.6, 0.97	0.05, 0.59, 0.98	164	163	249	250
28,29,30	0.0, 0.21, 0.86	0.0, 0.21, 0.87	85	87	249	250
31,32,33	0.0, 0.22, 0.86	0.0, 0.22, 0.87	85	87	249	250
34,35,36	0.2, 0.85, 1.0	0.19, 0.85, 1.0	164	163	546	541
37,38,39	0.2, 0.85, 1.0	0.19, 0.86, 1.0	164	163	546	541
40,41,42	0.08, 0.68, 0.98	0.08, 0.68, 0.99	85	87	546	541
43,44,45	0.08, 0.68, 0.98	0.08, 0.68, 0.99	85	87	546	541
46,47,48	0.0, 0.26, 0.94	0.0, 0.25, 0.95	164	163	249	250
49,50,51	0.0, 0.02, 0.73	0.0, 0.02, 0.74	85	87	249	250
52,53,54	0.02, 0.71, 1.0	0.01, 0.7, 1.0	164	163	546	541
55,56,57	0.0, 0.36, 0.96	0.0, 0.35, 0.97	85	87	546	541
Simulations at higher ambient temperatures						
58,59,60,61,62	0.03, 0.14, 0.44, 0.79, 0.94	0.02, 0.13, 0.43, 0.8, 0.95	177	176	110	112
63,64,65,66,67	0.0, 0.01, 0.09, 0.3, 0.69	0.0, 0.0, 0.09, 0.31, 0.7	92	95	110	112
68,69,70,71,72	0.08, 0.28, 0.67, 0.9, 0.98	0.07, 0.27, 0.67, 0.9, 0.99	177	176	262	263
73,74,75,76,77	0.0, 0.07, 0.27, 0.65, 0.89	0.0, 0.07, 0.27, 0.66, 0.9	92	95	262	263
78,79,80,81,82	0.05, 0.21, 0.57, 0.86, 0.97	0.05, 0.2, 0.56, 0.86, 0.97	186	185	163	163
83,84,85,86,87	0.0, 0.03, 0.15, 0.46, 0.81	0.0, 0.03, 0.15, 0.47, 0.82	97	99	163	163
88,89,90,91,92	0.05, 0.19, 0.53, 0.84, 0.96	0.04, 0.17, 0.52, 0.84, 0.96	191	191	123	121
93,94,95,96,97	0.0, 0.02, 0.12, 0.38, 0.76	0.0, 0.02, 0.12, 0.39, 0.77	99	102	123	121
98,99,100	0.04, 0.53, 0.96	0.04, 0.52, 0.96	191	191	123	121
101,102,103	0.05, 0.53, 0.96	0.04, 0.52, 0.97	191	191	123	121
104,105,106	0.0, 0.12, 0.76	0.0, 0.12, 0.77	99	102	123	121
107,108,109	0.0, 0.12, 0.76	0.0, 0.12, 0.77	99	102	123	121
110,111,112,113,114	0.04, 0.18, 0.52, 0.83, 0.96	0.04, 0.16, 0.5, 0.83, 0.96	195	194	102	99
115,116,117,118,119	0.0, 0.01, 0.1, 0.34, 0.73	0.0, 0.01, 0.1, 0.35, 0.74	101	104	102	99
Simulations with A320/B737-like aircraft						
120	0.72	0.72	164	163	176	183
121,122,123	0.13, 0.64, 0.96	0.12, 0.64, 0.97	177	176	76	79
124,125,126	0.03, 0.21, 0.78	0.03, 0.21, 0.8	92	95	76	79
127,128,129	0.2, 0.76, 0.99	0.19, 0.76, 0.99	177	176	185	186
130,131,132	0.07, 0.39, 0.9	0.06, 0.4, 0.91	92	95	185	186
133,134,135	0.17, 0.72, 0.98	0.16, 0.72, 0.98	186	185	114	113
136,137,138	0.04, 0.29, 0.85	0.04, 0.29, 0.86	186	185	114	113
139,140,141	0.16, 0.71, 0.97	0.15, 0.7, 0.98	191	191	85	83
142,143,144	0.04, 0.26, 0.82	0.03, 0.26, 0.83	99	102	85	83
145,146,147	0.16, 0.7, 0.97	0.15, 0.69, 0.98	195	194	70	67
148,149,150	0.03, 0.24, 0.81	0.03, 0.24, 0.82	101	104	70	67

Table S1. List of parametrized survival fractions derived with length scales that are computed via the numerical (Eqs. (6) and (7)) or the analytical method (Eqs. (A2) and (A3)), denoted with a tilde, and the corresponding length scales. Rows with three, five, or six simulations correspond to sets where the N_0-scaling factors 100, 1, 0.01; 100, 10, 1, 0.1, 0.01; or ~~100~~1000, 100, 10, 1, 0.1, 0.01 are applied, respectively.